

TESTING MODELS FOR MOLECULAR GAS FORMATION IN GALAXIES: HYDROSTATIC PRESSURE OR GAS AND DUST SHIELDING?

MICHELE FUMAGALLI¹, MARK R. KRUMHOLZ¹, AND LESLIE K. HUNT²

¹ Department of Astronomy and Astrophysics, University of California, 1156 High Street, Santa Cruz, CA 95064, USA; mfumagalli@ucolick.org

² INAF-Osservatorio Astrofisico di Arcetri, Largo E. Fermi 5, 50125 Firenze, Italy

Received 2010 March 7; accepted 2010 August 20; published 2010 September 23

ABSTRACT

Stars in galaxies form in giant molecular clouds that coalesce when the atomic hydrogen is converted into molecules. There are currently two dominant models based on the property of the galactic disk that determines its molecular fraction: either hydrostatic pressure driven by the gravity of gas and stars, or a combination of gas column density and metallicity. To assess the validity of these models, we compare theoretical predictions to the observed atomic gas content of low-metallicity dwarf galaxies with high stellar densities. The extreme conditions found in these systems are optimal for distinguishing the two models, otherwise degenerate in nearby spirals. Locally, on scales < 100 pc, we find that the state of the interstellar medium is mostly sensitive to the gas column density and metallicity rather than hydrostatic pressure. On larger scales where the average stellar density is considerably lower, both pressure and shielding models reproduce the observations, even at low metallicity. We conclude that models based on gas and dust shielding more closely describe the process of molecular formation, especially at the high resolution that can be achieved in modern galaxy simulations or with future radio/millimeter arrays.

Key words: galaxies: dwarf – galaxies: ISM – ISM: molecules – stars: formation

Online-only material: color figures

1. INTRODUCTION

Theoretical arguments based on gravitational instability as well as observations of molecular gas reveal that low-temperature ($T \sim 10$ K) and high-density ($n \sim 40 \text{ cm}^{-3}$) giant molecular clouds (GMCs) are the natural sites where stars form. Although individual GMCs can be resolved only in the Milky Way or in a handful of local galaxies (e.g., Bolatto et al. 2008, and references therein), CO observations of several nearby spirals show that star formation mostly occurs in molecular regions³ (e.g., Wong & Blitz 2002; Kennicutt et al. 2007; Bigiel et al. 2008). At the same time, neutral atomic hydrogen (HI) remains the primordial constituent of the molecular phase (H₂), playing an essential role in the formation of new stars, as shown by the low star formation rate (SFR; e.g., Boselli & Gavazzi 2006) and low molecular content (Fumagalli et al. 2009) found in HI-poor galaxies. Therefore, the transition from HI to H₂ is a key process that drives and regulates star formation in galaxies.

The problem of molecular formation has been studied extensively in the literature mainly through two different approaches. The first is by modeling the formation of molecular gas empirically, starting from CO and HI maps in nearby galaxies. Following this path, Wong & Blitz (2002, hereafter WB02), Blitz & Rosolowsky (2004, hereafter BR04), and Blitz & Rosolowsky (2006, hereafter BR06) have inferred that the molecular (Σ_{H_2}) to atomic (Σ_{HI}) surface density ratio

$$R_{\text{H}_2} = \Sigma_{\text{H}_2} / \Sigma_{\text{HI}} \quad (1)$$

in disks is a function solely of the hydrostatic midplane pressure P_{m} , which is driven both by the stellar and gas density: $R_{\text{H}_2} \sim P_{\text{m}}^{0.92}$ (hereafter BR model). The second approach

models the microphysics that regulates the formation of H₂ and its photodissociation. A detailed description should take into account the balance of H₂ formation onto dust grains and its dissociation by Lyman–Werner (LW) photons and cosmic rays, together with a complete network of chemical reactions that involves several molecules generally found in the interstellar medium (ISM). Due to this complexity, many studies address mainly the detailed physics of H₂ in individual clouds, without considering molecular formation on galactic scales (e.g., the pioneering work by van Dishoeck & Black 1986).

Elmegreen (1993) made an early attempt to produce a physically motivated prescription for molecule formation in galaxies by studying the HI to H₂ transition in both self-gravitating and diffuse clouds as a function of the external ISM pressure P_{e} and radiation field intensity j . This numerical calculation shows that the molecular fraction $f_{\text{H}_2} = \Sigma_{\text{H}_2} / \Sigma_{\text{gas}} \sim P_{\text{e}}^{2.2} j^{-1}$, with $\Sigma_{\text{gas}} = \Sigma_{\text{H}_2} + \Sigma_{\text{HI}}$. More recently, properties of the molecular ISM have been investigated with hydrodynamical simulations by Robertson & Kravtsov (2008) who have concluded that the H₂ destruction by the interstellar radiation field drives the abundance of molecular hydrogen and empirical relations such as the $R_{\text{H}_2} / P_{\text{m}}$ correlation. Using numerical simulations which include self-consistent metal enrichment, Gnedin et al. (2009) and Gnedin & Kravtsov (2010) have stressed also the importance of metallicity in regulating the molecular fraction and therefore the SFR. Similarly, Pelulessy et al. (2006) developed a subgrid model to track in hydrodynamical simulations the formation of H₂ on dust grains and its destruction by UV irradiation in the cold gas phase and collisions in the warm gas phase.

A different approach based entirely on first principles has been proposed in a series of papers by Krumholz et al. (2008, hereafter KMT08), Krumholz et al. (2009, hereafter KMT09), and McKee & Krumholz (2010, hereafter MK10). Their model (hereafter, the KMT model) describes the atomic-to-molecular transition in galaxies using a physically motivated prescription

³ Whether stars form from regions entirely dominated by molecules at the outskirts of disks remains an open question due to difficulties in probing molecular hydrogen via common tracers such as CO in those environments (e.g., Fumagalli & Gavazzi 2008; Leroy et al. 2008).

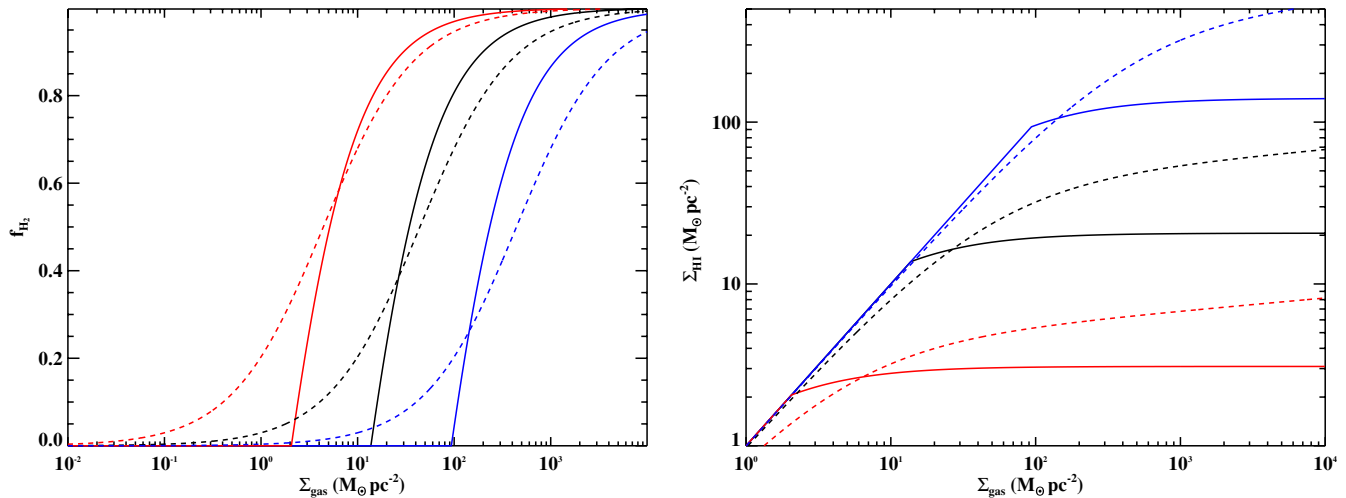


Figure 1. Left panel: molecular fractions computed for the KMT (solid lines) and BR (dashed lines) models. Different lines represent three metallicities for the KMT model (from right to left: $Z' = 0.1$, blue; $Z' = 1$, black; and $Z' = 10$, red) or three stellar densities for the BR model (from right to left: $\rho'_{\text{star}} = 0.001$, blue; $\rho'_{\text{star}} = 0.1$, black; and $\rho'_{\text{star}} = 10$, red). For the KMT model, we assume a clumping factor $c = 1$. Blue compact dwarfs (BCDs) at low metallicities and high stellar densities are the optimal systems to disentangle between the two models which are degenerate in massive spiral galaxies with solar metallicity (compare the two black lines). Right panel: models for the H I surface density as a function of the total gas column density, for the same parameters adopted in the left panel. While the KMT model exhibits a well-defined saturation in the atomic hydrogen, in the BR model Σ_{HI} increases asymptotically with Σ_{gas} . (A color version of this figure is available in the online journal.)

for the dust shielding and self-shielding of molecular hydrogen. This work differs from previous analyses mainly because it provides an analytic expression for f_{H_2} as a function of the total gas column density and metallicity (Z). Therefore, the KMT model can be used to approximate the molecular gas on galactic scales without a full radiative transfer calculation.

In this paper, we shall consider the BR and the KMT models as examples of the two different approaches used to describe the H I to H₂ transition in galaxies. Remarkably, both formalisms predict values for f_{H_2} which are roughly consistent with atomic and molecular observations in local disk galaxies (see Krumholz et al. 2009, Section 4.1.3). The reason is that the BR model becomes dependent on the gas column density alone if the stellar density is fixed to typical values found in nearby galaxies (see the discussion in Section 5). Despite the observed agreement, there are significant conceptual differences: the BR model is empirical and does not address the details of the ISM physics, while the KMT model approximates physically motivated prescriptions for the H₂ formation as functions of observables. Hence, although in agreement for solar metallicity at resolutions above a few hundred parsecs, the two prescriptions may not be fully equivalent in different regimes. It is still an open question whether molecule formation is mainly driven by hydrostatic pressure or UV radiation shielding over different spatial scales and over a large range of metallicities.

A solution to this problem has important implications in several contexts. From a theoretical point of view, cosmological simulations of galaxy formation that span a large dynamic range will benefit from a simple prescription for molecular gas formation in order to avoid computationally intense radiative transfer calculations. Similarly, semianalytic models or post-processing of dark-matter-only simulations will greatly benefit from a simple formalism that describes the molecular content in galaxies. Observationally, the problem of understanding the gas molecular ratio has several connections with future radio or millimeter facilities (e.g., ALMA, the Atacama Large Millimeter Array or SKA, the Square Kilometer Array). In fact, these interferometers will allow high-resolution

mapping of atomic and molecular gas across a large interval of redshift and galactic locations over which metallicity and intensity of the local photodissociating UV radiation vary significantly.

In this work, we explore the validity of the KMT and BR models in nearby dwarf starbursts both locally (<100 pc) and on larger scales (~ 1 kpc). Their low metallicity (down to a few hundredths of solar values) combined with the relatively high stellar densities found in these systems offers an extreme environment in which the similarity between the two models breaks down. In fact, for a fixed gas column density, high stellar density corresponds to high pressure and therefore high molecular fraction in the BR model. Conversely, for a fixed gas column density, low metallicity in the KMT model results in a low molecular fraction (see Figure 1).

We emphasize that the BR model was not designed to describe the molecular fraction on scales smaller than several hundred parsecs; indeed, Blitz & Rosolowsky (2006) explicitly warn against applying their model on scales smaller than about twice the pressure scale height of a galaxy. However, a number of theoretical models have extrapolated the BR model into this regime (e.g., Narayanan et al. 2010; Murante et al. 2010). The analysis we present at small scales (<100 pc, comparable to the resolutions of simulations in which the BR model has been used) is aimed at highlighting the issues that arise from such an extrapolation. Furthermore, a comparison of the pressure and shielding (KMT) models across a large range of physical scales offers additional insight into the physical processes responsible for the atomic-to-molecular transition.

The paper is organized as follows: after a brief review of the two models in Section 2, we will present two data sets collected from the literature in Section 3. The comparison between models and observations is presented in Section 4, while discussion and conclusions follow in Sections 5 and 6, respectively. Throughout this paper, we assume a solar photospheric abundance $12 + \log(\text{O}/\text{H}) = 8.69$ from Asplund et al. (2009). Also, we make use of dimensionless gas surface densities $\Sigma'_{\text{gas}} = \Sigma_{\text{gas}}/(M_{\odot} \text{pc}^{-2})$, stellar densities

$\rho'_{\text{star}} = \rho_{\text{star}}/(M_{\odot} \text{ pc}^{-3})$, gas velocity dispersions $v'_{\text{gas}} = v_{\text{gas}}/(\text{km s}^{-1})$, and metallicity $Z' = Z/Z_{\odot}$.

2. MODELS

Here, we summarize the basic concepts of the BR and KMT models which are relevant for our discussion. The reader should refer to the original works (WB02; BR04; BR06; KMT08; KMT09; MK10) for a complete description of the two formalisms.

2.1. The BR Model

The ansatz at the basis of the BR model is that the molecular ratio R_{H_2} is entirely determined by the midplane hydrostatic pressure P_{m} according to the power-law relation

$$R_{\text{H}_2} = \left(\frac{P_{\text{m}}}{P_{\odot}} \right)^{\alpha}. \quad (2)$$

The pressure can be evaluated with an approximate solution for the hydrostatic equilibrium for a two-component (gas and stars) disk (Elmegreen 1989):

$$P_{\text{m}} \sim G \Sigma_{\text{gas}} \left(\Sigma_{\text{gas}} + \Sigma_{\text{star}} \frac{v_{\text{gas}}}{v_{\text{star}}} \right), \quad (3)$$

where Σ_{star} is the stellar density, and v_{star} and v_{gas} are the stellar and gas velocity dispersion, respectively.

For a virialized disk, Equation (3) reduces to

$$P_{\text{m}} \sim \sqrt{G} \Sigma_{\text{gas}} v_{\text{gas}} \left(\Sigma_{\text{gas}}^{0.5} h_{\text{gas}}^{-0.5} + \Sigma_{\text{star}}^{0.5} h_{\text{star}}^{-0.5} \right); \quad (4)$$

by replacing the surface densities with volume densities using the disk scale heights h , the previous equation can be rewritten as

$$P_{\text{m}} \sim \sqrt{G} \Sigma_{\text{gas}} v_{\text{gas}} (\rho_{\text{gas}}^{0.5} + \rho_{\text{star}}^{0.5}). \quad (5)$$

Under the assumption that $\rho_{\text{star}} > \rho_{\text{gas}}$, the contribution of the gas self-gravity can be neglected and Equation (5) reduces to

$$\frac{P_{\text{m}}}{k} = 272 \Sigma'_{\text{gas}} (2\rho_{\text{star}})^{0.5} v'_{\text{gas}} \text{ K cm}^{-3}, \quad (6)$$

where $\Sigma'_{\text{gas}} = \Sigma_{\text{gas}}/(M_{\odot} \text{ pc}^{-2})$, $\rho'_{\text{star}} = \rho_{\text{star}}/(M_{\odot} \text{ pc}^{-3})$, and $v'_{\text{gas}} = v_{\text{gas}}/(\text{km s}^{-1})$. In deriving Equation (6), constants in cgs units have been added to match Equation (5) in BR06. Combining Equation (2) with Equation (6), the molecular ratio in the BR model becomes

$$R_{\text{H}_2} = [8.95 \times 10^{-3} \Sigma'_{\text{gas}} \rho_{\text{star}}^{0.5} v'_{\text{gas}}]^{0.92}, \quad (7)$$

where the best-fit values $P_{\odot} = (4.3 \pm 0.6) \times 10^4 \text{ K cm}^{-3}$ and $\alpha = 0.92$ have been derived from CO and H I observations of local spiral galaxies (BR06).

2.2. The KMT Model

The core of the KMT model is a set of two coupled integro-differential equations for the radiative transfer of LW radiation and the balance between the H_2 photodissociation and its formation onto dust grains. Neglecting the H_2 destruction by cosmic rays, the combined transfer-dissociation equation is

$$\vec{\nabla} \cdot \vec{F}^* = -n\sigma_{\text{d}}cE^* - \frac{f_{\text{H}_1}n^2\mathcal{R}}{f_{\text{diss}}}. \quad (8)$$

On the left-hand side, \vec{F}^* is the photon number flux integrated over the LW band. The first term on the right-hand side accounts for dust absorption, where n is the number density of hydrogen atoms, σ_{d} the dust cross section per hydrogen nucleus to LW-band photons, and E^* the photon number density integrated over the LW band. The second term accounts for absorption due to photodissociation, expressed in term of the H_2 formation rate in steady state conditions. Here, f_{H_1} is the hydrogen atomic fraction while f_{diss} is the fraction of absorbed radiation that produces dissociation rather than a de-excitation into a newly bound state. Finally, \mathcal{R} expresses the formation rate of molecular hydrogen on dust grains.

Equation (8) can be integrated for a layer of dust and a core of molecular gas mixed with dust. This solution specifies the transition between a fully atomic layer and a fully molecular core and hence describes the molecular fraction in the system as a function of the optical depth at which $F^* = 0$. Solutions to Equation (8) can be rewritten as a function of two dimensionless constants

$$\tau_{\text{R}} = n\sigma_{\text{d}}R \quad (9)$$

and

$$\chi = \frac{f_{\text{diss}}\sigma_{\text{d}}cE^*}{n\mathcal{R}}. \quad (10)$$

Here, τ_{R} is the dust optical depth for a cloud of size R , hence Equation (9) specifies the dimensions of the system. Conversely, χ is the ratio of the rate at which the LW radiation is absorbed by dust grains to the rate at which it is absorbed by molecular hydrogen.

To introduce these equations which govern the microphysics of the H_2 formation into a formalism that is applicable on galactic scales, one has to assume (Wolfire et al. 2003) that a cold-neutral medium (CNM) is in pressure equilibrium with a warm-neutral medium (WNM). Assuming further that dust and metals in the gas component are proportional to the total metallicity ($Z' = Z/Z_{\odot}$, in solar units), Equations (9) and (10) can be rewritten as a function of the observed metallicity and gas surface density. Using the improved formalism described in MK10, the analytic approximation for the molecular fraction as specified by the solutions of Equation (8) can be written as

$$f_{\text{H}_2} \simeq 1 - \left(\frac{3}{4} \right) \frac{s}{1 + 0.25s} \quad (11)$$

for $s < 2$ and $f_{\text{H}_2} = 0$ for $s \geq 2$. Here, $s = \ln(1 + 0.6\chi + 0.01\chi^2)/(0.6\tau_{\text{c}})$, $\chi = 0.76(1 + 3.1Z'^{0.365})$, and $\tau_{\text{c}} = 0.066\Sigma'_{\text{comp}}Z'$. Finally, $\Sigma'_{\text{comp}} = c\Sigma'_{\text{gas}}$ where the clumping factor $c \geq 1$ is introduced to compensate for averaging observed gas surface densities over scales larger than the typical scale of the clumpy ISM. Primed surface densities are in units of $M_{\odot} \text{ pc}^{-2}$.

2.3. Differences Between the Two Models

In Figure 1, we compare the BR and KMT models to highlight some behaviors that are relevant to our analysis. In the left panel, we present molecular fractions computed using the KMT (solid lines) and BR (dashed lines) formalisms. Different lines reflect three choices of metallicity for the KMT model (from right to left, $Z' = 0.1$ blue, $Z' = 1$ black, and $Z' = 10$ red) and three stellar densities for the BR model (from right to left, $\rho'_{\text{star}} = 0.001$ blue, $\rho'_{\text{star}} = 0.1$ black, and $\rho'_{\text{star}} = 10$ red). For a typical spiral disk with stellar mass $M_{\text{star}} = 10^{10} M_{\odot}$, size $R = 10 \text{ kpc}$, and stellar height $h = 300 \text{ pc}$, the stellar density is of the order of $\rho'_{\text{star}} \sim 0.1$. Figure 1 shows that, at solar

metallicity and for a typical gas surface density $\Sigma'_{\text{gas}} \sim 10\text{--}100$, the two models predict similar molecular fractions.

To break the degeneracy, we apply model predictions to observations of blue compact dwarf (BCD) galaxies or low-metallicity dwarf irregulars (dIrrs), characterized by high stellar density ($\rho'_{\text{star}} \sim 1\text{--}100$) and low metallicity ($Z' = 0.3\text{--}0.03$). In these environments, for a fixed gas surface density (excluding the limit $f_{\text{H}_2} \rightarrow 1$), the two models predict very different molecular to atomic ratios.

In the right panel of Figure 1, we show the predicted atomic gas surface density as a function of the total gas surface density, for the same parameters selected in the left panel. Besides the dependence on the metallicity and stellar density, this plot reveals a peculiar difference between the two models. The KMT formalism exhibits a well-defined saturation threshold in $\Sigma_{\text{H I}}$ for a fixed value of metallicity. This corresponds to the maximum H I column density that is required to shield the molecular complex from the LW-band photons. All the atomic hydrogen that exceeds this saturation level is converted into molecular gas. Conversely, the BR model has no saturation in the atomic gas surface density, but it increases slowly as the total gas surface density increases.

3. THE DWARF GALAXY SAMPLES

We study the behavior of the KMT and the BR models using two data sets compiled from the literature. Specifically, we have selected low-metallicity compact dwarf galaxies with sufficient observations to constrain gas densities, stellar masses, and metal abundances for a comparison with models. The first sample comprises 16 BCDs and dIrrs, for which quantities integrated over the entire galaxy are available. These objects constitute a low-resolution sample with which we study the two models on galactic scales (>1 kpc). For seven of these galaxies, we also have high-resolution H I maps and *Hubble Space Telescope* (*HST*) optical images. With these objects, we construct a high-resolution sample, useful to study the two formalisms at the scale of individual star cluster complexes (<100 pc).

Both models depend on the total gas surface density. In principle, we could use CO emission, available in the form of integrated fluxes from the literature, to quantify Σ_{gas} and the molecular content of individual galaxies. However, recent studies of molecular hydrogen traced through a gas-to-dust ratio (e.g., Imara & Blitz 2007; Leroy et al. 2009) support the idea that CO is a poor tracer of molecular hydrogen in low-metallicity environments, mostly due to its inability to self-shield (Wolfire et al. 2010). Therefore, CO seems an unreliable H_2 tracer for these metal-poor galaxies. For this unfortunate reason, we avoid any attempt to precisely quantify Σ_{H_2} , but rather use the observed H I column density as a lower limit on the total gas column densities.

As discussed in Section 2.3, the KMT model has a well-defined saturation threshold for $\Sigma_{\text{H I}}$, and this threshold constitutes an observationally testable prediction. The BR model does not have such a threshold and at a given ρ_{star} is in principle capable of producing arbitrarily high values of $\Sigma_{\text{H I}}$ provided that the total gas density Σ_{gas} is sufficiently high. However, the extremely weak variation of $\Sigma_{\text{H I}}$ with Σ_{gas} at large total gas column density ($\Sigma_{\text{H I}} \propto \Sigma_{\text{gas}}^{0.08}$) means that the amount of total gas required to produce a given $\Sigma_{\text{H I}}$ may be implausibly large. This effect allows us to check the BR model as well using only H I (Section 4), albeit not as rigorously as we can test the KMT model. We also check the robustness of our results in Appendix C, where we impose

an upper limit on Σ_{H_2} either from SFRs, assuming a depletion time $t_{\text{depl}} \sim 2$ Gyr (Bigiel et al. 2008) for molecular gas, or from CO fluxes, using a conservative CO-to- H_2 conversion.

In the next sections, we discuss in detail the procedures adopted to derive gas surface densities and stellar densities for the two samples. The reader not interested in these rather technical aspects can find the analysis, discussion, and conclusions starting from Section 4.

3.1. High-resolution Sample

Seven BCDs are found in the literature with high-resolution H I maps and with sufficient ancillary *HST* data to infer stellar masses on scales <100 pc, typical of individual GMCs. A detailed description of how we compute $\Sigma_{\text{H I}}$ and ρ_{star} in individual galaxies is provided in Appendix A, together with a list of relevant references. Here, we only summarize the general procedures we use.

Stellar masses of individual clusters are in a few cases directly taken from the literature. Otherwise, we infer stellar masses from integrated light by comparing two methods. The first is based on age estimates, whenever those are available in the literature. In this case, we infer stellar masses from observed absolute magnitudes by comparing the *K*- or *V*-band luminosity with predictions at the given age by Starburst99 (SB99; Leitherer et al. 1999). This is done assuming an instantaneous burst, similar metallicity, and a Salpeter initial mass function (IMF) with lower and upper mass limits at 1 and $100 M_{\odot}$, respectively. The second method is based on optical and near-infrared colors (e.g., $B - V$, $V - I$, $V - J$, $V - H$, $V - K$). In this case, we use mass-to-light (M/L) ratios inferred from colors (Bell & de Jong 2001), and the stellar masses are derived directly from observed luminosities. Usually, the two methods give similar results to within a factor of ~ 2 .

Once the masses are known, we obtain stellar densities with sizes taken from the literature. If not available, we measure them by fitting a two-dimensional elliptical Gaussian to the clusters in *HST* images. For the closest objects, in order to avoid resolving individual stars, we fit binned surface brightness profiles with a one-dimensional Gaussian.

Stellar masses are probably the most uncertain quantities in our study. In fact, our first method suffers from the rapid changes in the broadband output of a starburst at young ages (4–10 Myr), due to the onset of red supergiants whose amplitude and time of onset depend on metallicity. Moreover, the IMF of the SB99 models and the lower-mass cutoff may introduce additional uncertainty, up to a factor of 3, considering a full range of systematic uncertainties (Bell et al. 2003). Instead, sources of error in the second method are the strong contribution of nebular continuum and line emission to the broadband colors of young starbursts. This can be a particularly severe problem in the *K* band because of recombination lines and free-free emission which in some cases constitutes as much as 50% of the broadband *K* magnitude (see Vanzì et al. 2000; Hunt et al. 2001, 2003). Despite this rather large uncertainty on the stellar densities, the results presented in the next sections can be considered rather robust. In fact, a variation in the density larger than the uncertainty would be required to significantly alter our conclusions. A more extensive discussion on this issue is presented in Section 4.1.2.

To complete the data set, we add to the gas and stellar densities values for the metallicity, distances, and SFR indicators as collected from the literature. Individual references are provided in Appendix A and Tables 1 and 2. We derive integrated SFRs

Table 1
Data Set for the High-resolution Sample^a

Name	Distance (Mpc)	12 + log(O/H)	M_{star}^b ($10^5 M_{\odot}$)	Radius (pc)	ρ_{star}^b ($M_{\odot} \text{pc}^{-3}$)	Σ_{star}^b ($M_{\odot} \text{pc}^{-2}$)	$\Sigma_{\text{H I}}$ (10^{21}cm^{-2})	Σ_{sfr} ($M_{\odot} \text{yr}^{-1} \text{kpc}^{-2}$)
IZw 18	13	7.19	4.7	56	0.64	47.9	3.5	0.134
			2.3	56	0.31	23.3		
SBS 0335 – 052	53.7	7.23	10	18.2	39.5	959	7	0.154
			11		43.4	1055		
			4		15.8	384		
			11		43.4	1055		
			18		71.0	1726		
Mrk 71	3.44	7.90	0.12	7.2	7.7	74	6	0.214
			0.054		3.5	33		
UM 462	15.3	7.98	3.5–7.2	21	9–19	255–520	5.7	0.060
			1.2–2.2	27.5	1.4–2.5	51–92		
			2.1	43	0.6	36		
			1.8	27.5	2	74		
			1.6–2.9	33	1–2	48–85		
II Zw 40	10.3	8.13	6.4–12	10.1	149–280	2005–3759	7.9	4.610
			1.3–15	5.2	222–2550	1536–17730		
NGC 5253	3.5	8.19	0.13	3.0	115	460	6.4	0.181
			0.7–4	1.6–2.9	3915–4080	8704–15140		
			10–13	3.5	5570–7240	25980–33780		
NGC 1140	18.2	8.20	9.1	7.3	558	5436	2.5	0.024
			59	6.6	4899	43114		

Notes.

^a Individual references are provided in Appendix A, together with a detailed description of how quantities are measured. Metallicities and SFRs are the same as those given in Table 2.

^b For the most uncertain values, we report the upper and lower limits. See Appendix A for further details.

using $\text{H}\alpha$, 60 μm , and radio free–free fluxes as different tracers. The final rates are given assuming the empirical calibrations by Kennicutt (1998) for the $\text{H}\alpha$, by Hopkins et al. (2002) for the 60 μm , and by Hunt et al. (2005a) for the radio free–free emission. We note that this last tracer is optimum in the absence of non-thermal emission, as typical in young starbursts. Since SFRs are used to set an upper limit on the total gas density assuming a given depletion time (Appendix C), we choose the maximum value whenever more than one indicator is found for a single galaxy. Total SFR surface densities are then calculated adopting the galaxy sizes from NED.⁴ A summary of the collected and derived data is presented in Table 1.

The stellar densities in the high-resolution sample are generally quite high, and associated with massive compact star clusters, some of which are in the super star cluster (SSC) category (e.g., O’Connell et al. 1994; Meurer et al. 1995; Whitmore et al. 2005). Despite their extreme properties, none of the BCDs in the high-resolution sample exceed the maximum stellar surface density limit found by Hopkins et al. (2010), and most are 5–10 times below this limit. Interestingly, the stellar densities here are uncorrelated with metallicity, implying that some other parameter must play the main role in defining the properties of massive star clusters.

3.2. Low-resolution Sample

We have collected a second sample from the literature by requiring only that quantities integrated over the entire galaxy be available. Due to the lower spatial resolution, this data set is suitable to study the KMT and BR models on larger scales

(>1 kpc). Our search yielded a total of 16 low-metallicity star-forming galaxies; among these are the seven objects in the high-resolution sample. We have compiled gas and stellar densities, distances, and metallicity for these 16 objects, most of which are classified as BCDs, but some are dlrrs (Sm, Im), since they are more diffuse, larger in size, and more luminous (massive) than typical BCDs.

Stellar masses are computed from *Spitzer*/IRAC fluxes following the formulation of Lee et al. (2006), as we summarize in Appendix B, together with a comment on the dominant sources of uncertainty. Stellar densities are then derived assuming spherical symmetry and the sizes inferred from the stellar component, as measured from IRAC images. The resolution of these images ($\sim 1''/2$) is a factor of 10 lower than the worst *HST* resolution, so that the compact regions are unresolved. This implies that the stellar densities derived for this sample are much lower than the values quoted for individual star cluster complexes. Moreover, for non-spherical (spheroidal) BCDs these densities correspond formally to lower limits; the volume of a prolate spheroid is smaller than the volume of a sphere by a factor $(b/a)^{0.5}$, with a and b the semimajor and semiminor axes, respectively. In our sample, the mean axis ratio is $a/b \sim 1.5$ with a 0.5 standard deviation. This discrepancy is small enough to justify our assumption of spherical symmetry. In any case, the possible volume overestimate could partially compensate the potential overestimate of stellar density because of nebular emission contamination or free–free emission (see the discussion in Appendix B).

For most objects, integrated H I fluxes are retrieved from HyperLeda⁵ (Paturel et al. 2003). We then convert integrated

⁴ NASA/IPAC Extragalactic Database.

⁵ <http://leda.univ-lyon1.fr>

Table 2
Data Set for the Low-resolution Sample

Name	Distance (Mpc)	$12 + \log(\text{O}/\text{H})^{\text{a}}$	Diameter ^b (kpc)	M_{star} (Min-avg) ($\log M_{\odot}$)	$\Sigma_{\text{H I}}^{\text{c}}$ ($M_{\odot} \text{ pc}^{-2}$)	CO Flux ^d (K km s^{-1})	$\Sigma_{\text{sfr}}^{\text{e}}$ ($M_{\odot} \text{ yr}^{-1} \text{ kpc}^{-2}$)	SFR Tracer
Haro3	16.8	8.30	5.23–4.79	9.09–9.35	10.2	1.98	0.106	60 μm
IIZw 40	10.3	8.12	2.80–1.04	8.09–8.34	91.4	0.50	4.610	ff
IZw 18	13.0	7.19	1.44–0.93	6.51–6.88	39.3	< 1.00	0.134	ff
Mrk 209	5.4	7.81	1.16–1.09	7.29–7.36	14.2	0.45	0.051	H α
Mrk 33	24.9	8.45	7.61–6.86	9.59–9.79	4.3	6.21	0.103	60 μm
Mrk 71	3.4	7.90	0.81–0.81	6.54–6.89	12.4	< 0.34	0.214	H α
NGC 1140	18.2	8.20	6.56–6.55	9.30–9.58	15.7	0.97	0.024	H α
NGC 1156	7.1	8.23	5.53–5.93	8.62–9.10	5.0	0.76	0.007	H α
NGC 1741	55.1	8.05	17.82–22.44	9.29–9.81	9.7	1.53	0.040	60 μm
NGC 2537	8.0	8.19	4.48–3.72	9.14–9.26	5.4	0.56	0.013	H α
NGC 4214	3.3	8.20	2.91–7.19	8.66–8.67	2.3	0.90	0.003	H α
NGC 5253	3.5	8.19	3.29–3.14	8.63–9.05	2.7	0.73	0.181	ff
NGC 7077	13.3	8.04	2.72–2.90	8.54–8.60	3.6	0.68	0.014	H α
SBS 0335 – 052	53.7	7.23	4.24–3.35	7.79–8.72	24.5	< 5.43	0.154	H α
UM 448	81.2	8.00	15.67–8.18	10.30–10.69	34.1	0.82	0.669	60 μm
UM 462	15.3	7.97	2.48–2.44	7.95–8.20	16.1	0.55	0.060	60 μm

Notes.

^a References for metallicity: Davidge 1989; Campos-Aguilar et al. 1993; Izotov et al. 1997; Gil de Paz et al. 2002; Izotov & Thuan 2004a; Thuan & Izotov 2005; van Zee & Haynes 2006.

^b Diameters as computed from stellar profiles and derived from NED.

^c References for H I: HyperLeda except for I Zw 18 and Mrk 71, as described in the text.

^d References for CO: Sage et al. 1992; Leon et al. 1998; Taylor et al. 1998; Barone et al. 2000; Dale et al. 2001; Gil de Paz et al. 2002; Albrecht et al. 2004; Leroy et al. 2005; Leroy et al. 2007.

^e References for SFR: Young et al. 1989; Drissen et al. 2000; Hopkins et al. 2002; Gil de Paz et al. 2002; Hunt et al. 2004; Izotov & Thuan 2004a; Hunt et al. 2005a; Hunt et al. 2005b; Schmitt et al. 2006; van Zee & Haynes 2006.

fluxes into mean column densities using optical radii from NED, and assuming that the gas extends twice as far as the stellar component (see Lee et al. 2002; van Zee et al. 1998b; Thuan et al. 2004). For I Zw 18, the integrated H I flux is not available in HyperLeda and we consider the flux published in de Vaucouleurs et al. (1991). Similarly, for Mrk 71 we estimate the total atomic gas from available interferometric observations averaged over the entire galaxy (Thuan et al. 2004).

¹²CO(1–0) fluxes are available for most of the galaxies here considered (see Table 2). For three galaxies, the most metal-poor objects in our sample (SBS 0335–052 E, I Zw 18, and Mrk 71), we find only CO upper limits in the literature. Because we use CO fluxes only to set upper limits on Σ_{H_2} (Appendix C), we choose one of the largest CO-to-H₂ conversion measured to date (Leroy et al. 2009). It is worth noting that for extremely metal-poor galaxies (e.g., I Zw 18) the adopted conversion factor may still underestimate the H₂ content. To make our limits even more conservative, we compare these values with Σ_{H_2} inferred from SFRs and we choose for each galaxy the maximum of the two.

As with the high-resolution sample, we derive SFRs from H α , 60 μm , or free–free emission (see Table 2 for references). Again, SFR densities are computed assuming the optical size as given by NED. Finally, we collect information on the metallicity and distances for each object. A summary of the data derived for the low-resolution sample is given in Table 2.

4. ANALYSIS

4.1. Testing Models on Small Scales (<100 pc)

With the aim of testing how the BR and KMT models perform at high stellar density and low metallicity, we first compare both formalisms with the observed H I surface densities and stellar densities in the high-resolution data set. Since the average resolution of this sample is below 100 pc, this part of the analysis

focuses mainly on the molecular fraction in individual GMCs and associations rather than on larger ISM spatial scales. As previously mentioned, the BR formalism was not developed to describe the molecular fraction in such small regions (BR06). Hence, the results presented in this section are intended to assess possible pitfalls of extrapolating the pressure model to small scales. Furthermore, a comparison of the performances of the BR and KMT models below 100 pc provides insight into what quantities are relevant to the production of molecules on different size scales.

As summarized in Section 2.2, the KMT formalism describes the molecular fraction as a function of the total gas column density and metallicity. A free parameter is the clumping factor c that maps the observed column density Σ_{gas} onto the relevant quantity in the model, i.e., the column density of the cold phase in individual clouds. With resolutions coarser than ~ 100 pc, beam smearing dilutes the density peaks and one must adopt $c > 1$ in order to recover the intrinsic gas surface density $\Sigma_{\text{comp}} = c\Sigma_{\text{gas}}$. However, given the high resolution of the *HST* images, we set $c = 1$ so that the KMT model has no free parameters.

Conversely, as reviewed in Section 2.1, the BR model describes R_{H_2} as function of the total column density and stellar volume density. An additional parameter in this case is the gas velocity dispersion, set to $v'_{\text{gas}} = 8$. Apart from a similar dependence on Σ_{gas} , a direct comparison between models and observations is not straightforward. We start our analysis by confronting each model with observations, and then attempt a comparison of both models and data.

4.1.1. The KMT Model Predictions Below 100 pc

In Figure 2, we present the observed H I surface density (crosses) together with predictions from the KMT model (lines)

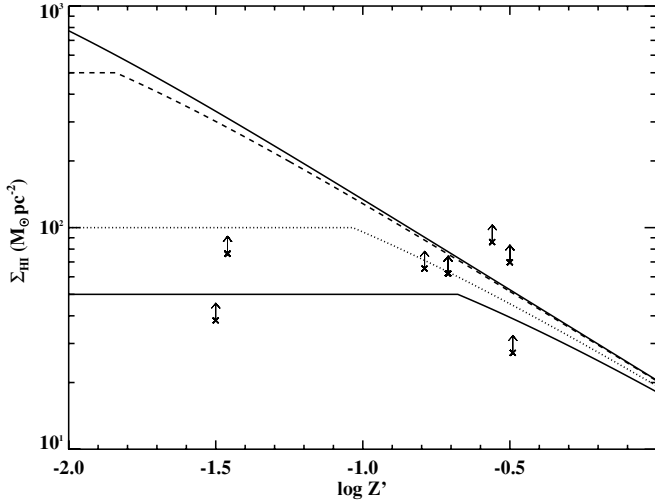


Figure 2. Comparison between observations of the H I surface density (crosses) with prediction from the KMT model (lines) as a function of the metallicity. Different curves are computed for different total gas column densities ($\Sigma'_{\text{gas}} = 50$ solid line, $\Sigma'_{\text{gas}} = 10^2$ dotted line, $\Sigma'_{\text{gas}} = 5 \times 10^2$ dashed line, and $\Sigma'_{\text{gas}} = 10^3$ dash-dotted line). The KMT model is computed for $c = 1$ and H I data are shown as lower limits since they are averaged over regions which are more extended than 100 pc (see the text for further details). Observations do not rule out the KMT model since there is a significant overlap between the parameter space allowed by both the theoretical curves and the data.

as a function of the metallicity. Different curves are computed for different total gas column densities ($\Sigma'_{\text{gas}} = 50$ solid line, $\Sigma'_{\text{gas}} = 10^2$ dotted line, $\Sigma'_{\text{gas}} = 5 \times 10^2$ dashed line, and $\Sigma'_{\text{gas}} = 10^3$ dash-dotted line). Here, and for the rest of this analysis, we correct the gas column density for helium with a standard coefficient 1.36. We do not include corrections for projection effects because in dwarf galaxies a unique inclination angle is not well defined for a warped (non-planar) H I distribution or in a triaxial system.

As discussed in Appendix A, interferometric H I observations do not achieve the resolution required to match the *HST* observations. A possible solution is to downgrade *HST* images to match the atomic hydrogen maps. However, since the exact value for c would be unknown at the resultant resolution ($\gtrsim 100$ pc), we perform our analysis on scales < 100 pc, compatible with *HST* images and where $c \rightarrow 1$. For this reason, we express the observed H I column density as lower limits on the local $\Sigma_{\text{H I}}$. This is because coarser spatial resolutions most likely average fluxes on larger areas, thus lowering the inferred peak column density. Indeed, whenever H I observations at different resolutions are compared, better resolution is associated with higher column densities. SBS 0335–052 E is an example: this BCD has $\Sigma_{\text{H I}} = 7.4 \times 10^{20} \text{ cm}^{-2}$ in a beam of $20''.5 \times 15''.0$ (Pustilnik et al. 2001) and $2 \times 10^{21} \text{ cm}^{-2}$ in a $3''.4$ beam (Ekta et al. 2009). The inferred H I column density is even higher, $7 \times 10^{21} \text{ cm}^{-2}$, with the smaller $2''$ beam in *HST*/GHRS observations of Ly α absorption (Thuan & Izotov 1997).

In any case, the lower limits illustrated in Figure 2 prevent us from concluding that model and observations are in complete agreement, although this is strongly suggested. Adopting a conservative approach, this comparison shows that observations do not immediately rule out the KMT model on scales of < 100 pc; 5/7 of the galaxies here considered are consistent with predicted curves. Although not crucial for the current and remaining analysis, the quoted metallicity may in some cases overestimate the dust and metal content which contributes to

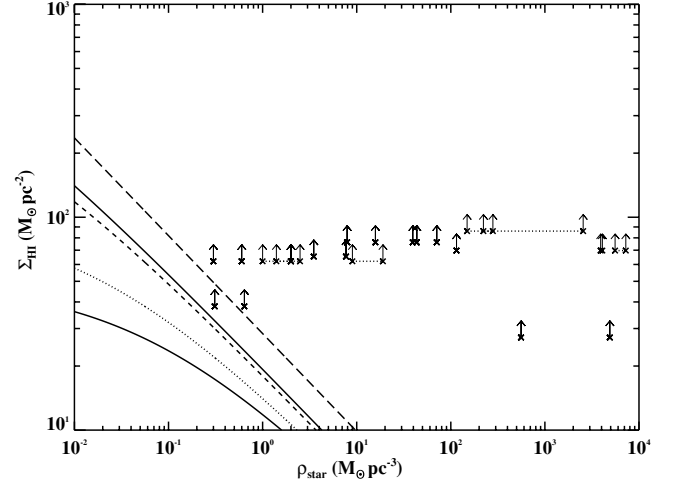


Figure 3. Comparison between the predicted $\Sigma_{\text{H I}}$ from the BR model (lines) and observations (crosses) as a function of the stellar density in individual GMCs and associations. Different curves are for choices of total gas density ($\Sigma'_{\text{gas}} = 50$, solid line; $\Sigma'_{\text{gas}} = 10^2$, dotted line; $\Sigma'_{\text{gas}} = 5 \times 10^2$, dashed line; $\Sigma'_{\text{gas}} = 10^3$, dash-dotted line; and $\Sigma'_{\text{gas}} = 10^4$, long-dashed line). Observed H I column densities are represented as lower limits on the local atomic gas column density (see the text for further details). Observations rule out the BR model once extrapolated below 100 pc.

the H₂ formation. In fact, in the KMT model, it is the CNM that plays a relevant role in regulating f_{H_2} and the assumption that the nebular metallicity reflects the metal abundances in the cold ISM may not hold in all cases. Specifically, the optically inferred metallicity used here is dominated by the ionized phase. Studies of the metal enrichment of the neutral gas in metal-poor dwarfs show that the neutral phase can be sometimes less metal enriched than the ionized medium (e.g., Thuan et al. 2005; Lebouteiller et al. 2004; Lecavelier des Etangs et al. 2004). Furthermore, galaxies with the lowest nebular metallicities have similar neutral gas abundances, while dwarfs with higher ionized nebular metallicities can have up to ~ 7 times (Lebouteiller et al. 2009) lower neutral ISM abundances (see however Bowen et al. 2005). A recent interpretation for this effect is that although mixing is effective in diffusing new metals from ionized regions, due to the larger volume, the enrichment is modest (Lebouteiller et al. 2009). This justifies the use of a single metallicity for multiple GMCs since, in the worst case, we would overestimate by some factor the local metal content. Data points, especially the ones at higher metallicity, would be offset to lower values and the parameter space common to data and model would increase, mitigating the discrepancy found at $Z' \sim -0.5$.

4.1.2. The BR Model Predictions Below 100 pc

Turning our attention to the BR model, we test predictions (lines) against the observed $\Sigma_{\text{H I}}$ (crosses) in Figure 3. Stellar densities are available for individual GMCs measured from high-resolution *HST* images. Therefore, while multiple observations overlap in metallicity in Figure 2, here we show distinct data points for the same galaxy. Once again, different curves are for a selection of total gas density ($\Sigma'_{\text{gas}} = 50$, solid line; $\Sigma'_{\text{gas}} = 10^2$, dotted line; $\Sigma'_{\text{gas}} = 5 \times 10^2$, dashed line; $\Sigma'_{\text{gas}} = 10^3$, dash-dotted line; and $\Sigma'_{\text{gas}} = 10^4$, long-dashed line); observed H I column densities are represented as lower limits on the local atomic gas column density. When stellar densities are particularly uncertain (see discussion in Appendix A), we plot both lower and upper limits connected with a dotted line.

According to the BR model, despite the low metallicity, a high fraction of hydrogen is expected to be molecular because of the enhanced stellar density. However, Figure 3 illustrates that observations discourage the use of pressure models on scales < 100 pc. Even under the very conservative hypothesis that stellar densities are overestimated by a factor of 2–3 and that the total column densities can reach very high values (e.g., the long-dashed curve at $\Sigma'_{\text{gas}} = 10^4$), observations mostly lie in the region not allowed by the extrapolation of the BR model.⁶ Compatibility between the extrapolation of the BR model and a good fraction of the data would require $\Sigma_{\text{gas}} \gtrsim 10^{10} M_{\odot} \text{pc}^{-2}$. A value that large would correspond to $A_V > 10^5$ with a dust-to-gas ratio that is 1% of the Milky Way value, and is thus ruled out by the fact that the star clusters are observable. Moreover, such a large Σ_{gas} would make the gas mass in the observed region larger than either the baryonic or the dark-matter mass of the entire dwarf galaxy. Clearly, even though we cannot directly detect the molecular component of the gas, we can rule out the presence of such a large amount of gas on other grounds, and we can therefore conclude that the extrapolated BR model is incompatible with the observations. We give a more rigorous estimate of the maximum plausible value of Σ'_{gas} in Appendix C.

An additional tunable parameter in the BR model is the gas velocity dispersion and a substantial change in v_{gas} can affect its predictions. In this paper, following BR04 and BR06, we adopt $v'_{\text{gas}} = 8$. Since pressure varies linearly with the velocity dispersion, we can solve for the value of v_{gas} required for the BR model to match the observations. We find that $v'_{\text{gas}} \lesssim 2$ in order to have one half of the data points consistent with the model; this is in contrast with recent H I observations (e.g., Chung et al. 2009; Walter et al. 2008) that show typical dispersion velocities $v'_{\text{gas}} > 5$ (and in many cases $v'_{\text{gas}} > 10$) in all the surveyed galaxies. It is worth mentioning that the use of the observed v_{gas} is not always appropriate, although unavoidable; for example, v_{gas} depends on the thermal velocity and the gas in a cold medium has a lower velocity dispersion than what inferred from a multiphase ISM. We conclude that the disagreement found in Figure 3 cannot be explained with uncertainties on the velocity dispersion.

Finally, we should assess if the high pressure predicted by the model can be attributed to the use of hydrostatic equilibrium in a disk rather than in a sphere, which would be more appropriate for our systems. Intuitively, this is not the case since the central pressure in a sphere of gas and stars cannot be lower than the midplane pressure of the disk. In fact, the central point in a sphere has to support the weight of the entire system, while each point in the midplane of a disk has to support only the pressure from the components along the vertical direction. This argument is substantiated by a quantitative analysis. A solution of the hydrostatic equilibrium equation for a sphere of gas and stars shows that the central gas pressure is enhanced by a quantity that depends on $(v_{\text{star}}/v_{\text{gas}})^2$. Therefore, to minimize an increase in the pressure due to the stellar component, the condition $(v_{\text{star}}/v_{\text{gas}}) \sim 1$ has to be satisfied. However, an increase in v_{gas} is reflected by an increase in the gas pressure itself. In other words, the central pressure in a gas sphere with cold kinematics (low v_{gas}) receives a significant contribution from the stellar potential

⁶ One might attempt to improve the agreement data model by artificially smearing the stellar density down to the same resolution as the H I observations (while ignoring the presence of additional stars outside the *HST* PSF). This brings the total gas surface density required to match the majority of the observations down to $\Sigma'_{\text{gas}} \sim 10^3\text{--}10^4$, still a very large value.

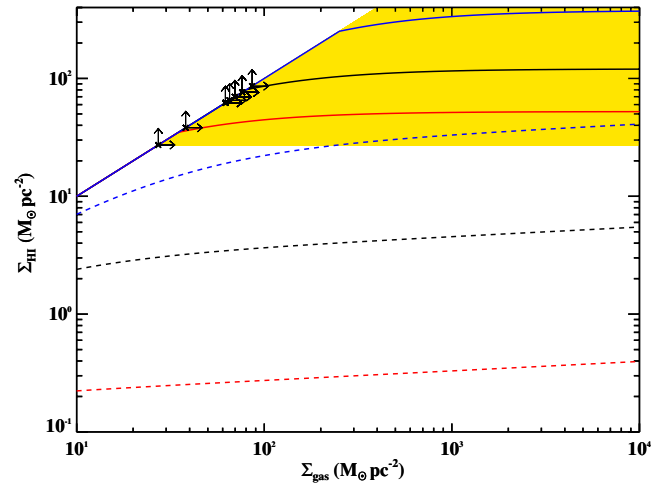


Figure 4. KMT model (solid lines) and BR model (dashed lines) as a function of the total gas density. Different curves are for the maximum, central, and minimum observed values of metallicity (in the KMT model: $Z' = 0.32$, red; $Z' = 0.12$, black; and $Z' = 0.03$, blue) and stellar density (in the BR model: $\log \rho'_{\text{star}} = 3.86$, red; $\log \rho'_{\text{star}} = 1.38$, black; and $\log \rho'_{\text{star}} = -0.52$, blue). Observed lower limits on $\Sigma_{\text{H I}}$ are superimposed. The yellow-shaded region encloses the largest parameter space allowed by observations. Data rule out any extrapolation of the BR model below 100 pc, where it largely overestimates the molecular fraction. Conversely, observations do not rule out immediately the KMT model.

(A color version of this figure is available in the online journal.)

($v_{\text{star}}/v_{\text{gas}} > 1$), while a gas sphere with hot kinematics (high v_{gas}) has an intrinsically higher gas pressure ($v_{\text{star}}/v_{\text{gas}} < 1$).

4.1.3. A Direct Comparison Between the Two Models

A different way to visualize both the models and the observations for the high-resolution sample is shown in Figure 4, where we plot predictions for $\Sigma_{\text{H I}}$ of the KMT model (solid lines) and the BR model (dashed lines) as a function of the total gas column density. Different curves in the KMT model are for the maximum, central, and minimum metallicity observed in the sample (from the bottom to the top, $Z' = 0.32$, red; $Z' = 0.12$, black; and $Z' = 0.03$, blue). The curves for the BR model correspond to the maximum, central, and minimum stellar density (from the bottom to the top, $\log \rho'_{\text{star}} = 3.86$, red; $\log \rho'_{\text{star}} = 1.38$, black; and $\log \rho'_{\text{star}} = -0.52$, blue). As in the previous figures, observed lower limits on $\Sigma_{\text{H I}}$ are superimposed. The yellow-shaded region in Figure 4 indicates the maximum parameter space allowed by the observations. This plot summarizes the two main results presented in the previous paragraphs. Observations of $\Sigma_{\text{H I}}$ reveal that an extrapolation of the BR model below scales of 100 pc results in a significant overestimation of the molecular fraction. In fact, for the observed $\Sigma_{\text{H I}}$, exceedingly high total gas surface densities ($\Sigma'_{\text{gas}} > 10^4$) are required by the BR model to reproduce observations. As shown quantitatively in Appendix C, such high values appear to be unrealistic. Conversely, observations seem to suggest a good agreement between the KMT model and data. Also, comparing Figure 4 with Figure 1, it appears that the different behavior of the two models for a similar gas column density is related to which quantity regulates the molecular fraction at the second order, subordinately to the gas column density. In fact, the discrepancy with observations and the BR model is associated with the high values of stellar densities, while the consistency between the observed H I column densities and the KMT model

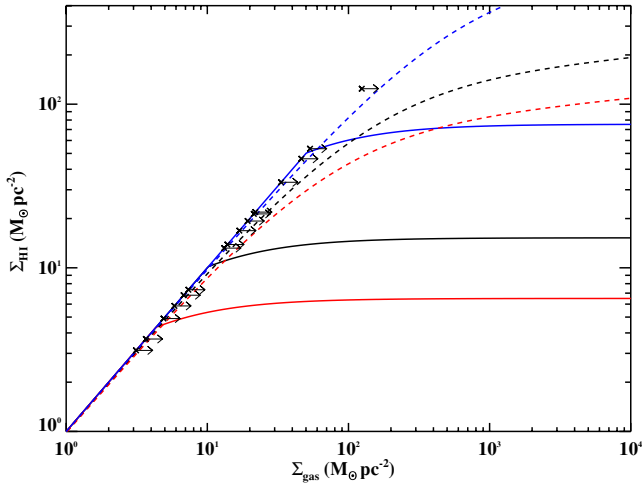


Figure 5. Comparison of the models with data in the low-resolution sample. Solid lines are for the KMT formalism, for the maximum ($Z' = 0.58$, red), central ($Z' = 0.20$, black), and minimum ($Z' = 0.03$, blue) observed metallicity. Dashed lines are for the BR model, for the maximum ($\log \rho'_{\text{star}} = -1.45$, red), central ($\log \rho'_{\text{star}} = -2.00$, black), and minimum ($\log \rho'_{\text{star}} = -3.18$, blue) stellar density in the sample. Lower limits on the total column density are for $\Sigma_{\text{gas}} = \Sigma_{\text{H I}}$. At low resolution, stellar densities drop by orders of magnitude and both models appear to be consistent with the data.

(A color version of this figure is available in the online journal.)

is fostered by the low value of metallicity that raises the atomic hydrogen saturation limit.

4.2. Testing Models on Galactic Scales (>1 kpc)

In the second part of this analysis, we compare predictions from models and observations on larger scales (>1 kpc), by considering spatially integrated quantities for a larger sample of BCDs. Before we start, it is worth mentioning that the condition $\Sigma'_{\text{star}} \gtrsim 20$ (see BR04) which ensures the validity of Equation (6) holds also for the low-resolution data set.

4.2.1. A Comparison Between Models and Global Data

In Figure 5, we present a comparison between observed H I surface densities and models, as previously done in Figure 4 for the high-resolution sample. Solid lines represent the KMT model, for the maximum ($Z' = 0.58$, red), central ($Z' = 0.20$, black), and minimum ($Z' = 0.03$, blue) observed metallicity. Dashed lines are for the BR model for the maximum ($\log \rho'_{\text{star}} = -1.45$, red), central ($\log \rho'_{\text{star}} = -2.00$, black), and minimum ($\log \rho'_{\text{star}} = -3.18$, blue) stellar density. Lower limits on the total gas column density are computed for $\Sigma_{\text{gas}} = \Sigma_{\text{H I}}$ (see Appendix C for a version of this figure that includes upper limits).

A comparison of Figures 5 and 4 reveals that the BR model predicts for the galaxy as a whole a much higher H I surface density, compared with the predictions for regions smaller than 100 pc. By going from the high-resolution sample to the low-resolution one, we lose the ability to analyze the local structure of the ISM, and are limited to average quantities which dilute the density contrasts in both gas and stars over many GMC complexes and aggregations. As a result, $\Sigma_{\text{H I}}$ and ρ_{star} are lowered by one and two orders of magnitude, respectively. This behavior is reflected in the BR model as a decrease in the pressure by an order of magnitude, which now guarantees an overall agreement between data and the model. Conversely, the beam smearing is accounted for in the KMT model by the clumping factor, here assumed to be $c \sim 5$. Hence, despite the

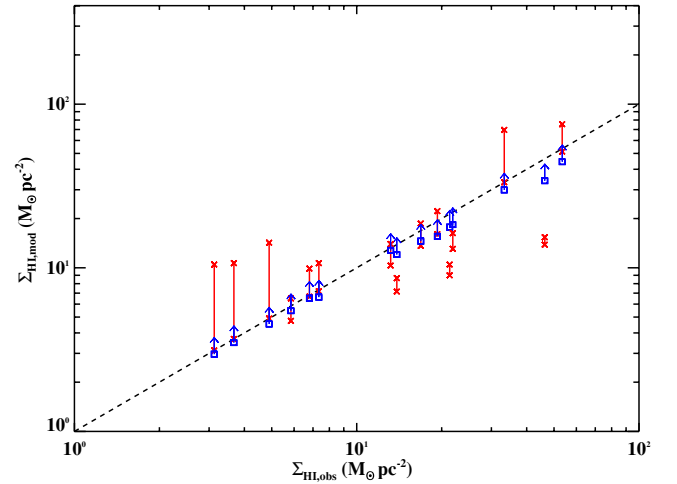


Figure 6. Predicted H I surface densities ($\Sigma_{\text{H I,mod}}$) computed either with observed metallicity using the KMT model (red crosses) or with stellar density using the BR model (blue squares) are shown as a function of the observed values ($\Sigma_{\text{H I,obs}}$) in individual galaxies. For the KMT model, lines connect lower and upper limits on $\Sigma_{\text{H I,mod}}$, derived assuming proper limits on Σ_{gas} from the saturation threshold. The BR model is consistent with observations in individual galaxies, even at low metallicity. Similarly, the KMT formalism can account for most of the galaxies, but fail to reproduce observations in some cases.

(A color version of this figure is available in the online journal.)

different spatial scales, the KMT formalism is able to account for the mean observed $\Sigma_{\text{H I}}$.

4.2.2. A Test with Individual Galaxies

Although indicative of a general trend, Figure 5 does not allow a comparison of individual galaxies with models. This is particularly relevant for the KMT formalism that predicts a saturation in the H I column density as a function of the metallicity. To gain additional insight, we present in Figure 6 the predicted H I surface density ($\Sigma_{\text{H I,mod}}$) against the observed one ($\Sigma_{\text{H I,obs}}$) for individual galaxies. For the KMT model, we compute $\Sigma_{\text{H I,mod}}$ using observed metallicities (red crosses). Since the total gas column density is unknown, we compute for each galaxy a range of $\Sigma_{\text{H I,mod}}$ (shown with solid red lines) using upper and lower limits on the observed total gas surface density. Lower limits are derived assuming $\Sigma_{\text{gas}} = \Sigma_{\text{H I,obs}}$, while upper limits arise self-consistently from the H I saturation column density, naturally provided by the model. For the BR model, we instead compute only lower limits on $\Sigma_{\text{H I,mod}}$ with stellar densities (blue squares), assuming $\Sigma_{\text{gas}} = \Sigma_{\text{H I,obs}}$ (upper limits derived for $\Sigma_{\text{H I,mod}}$ are presented in Appendix C).

From Figure 6, the asymptotic behavior of $\Sigma_{\text{H I}}$ in the BR model prevents a tighter constraint on Σ_{gas} . In general, there is good agreement between observations and model predictions for all the galaxies, despite the low mean metallicity of this sample. Conversely, the KMT model allows a narrower interval of H I surface density because of the well-defined atomic hydrogen saturation. Therefore, Figure 6 provides a more severe test of the KMT formalism that nevertheless reproduces correctly most of the observations. Although for 4/16 galaxies the KMT predictions are inconsistent with the data, there seems to be no peculiar reason for the failure of the model for these objects (see Section 4.2.3).

For many objects, the agreement between models and observations occurs close to the lower limits on $\Sigma_{\text{H I,mod}}$, i.e., when $\Sigma_{\text{gas}} = \Sigma_{\text{H I}}$. We stress that this is not an obvious outcome of the assumption made on the total gas surface density, since high

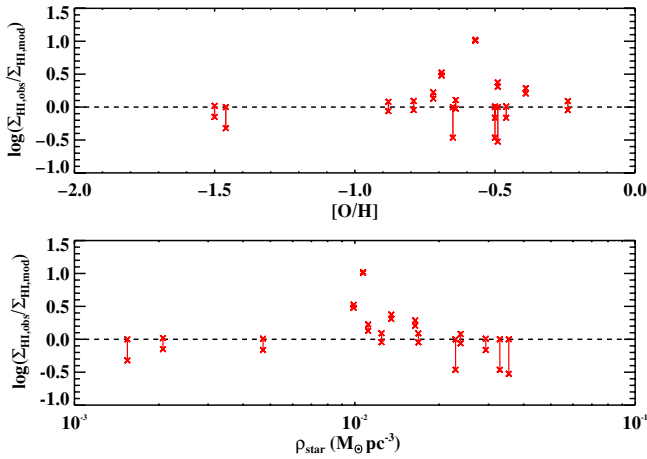


Figure 7. Ratio of the observed and predicted H I surface densities in the KMT model (red crosses) as a function of metallicity (upper panel) and stellar density (lower panel). The two dashed horizontal lines indicate the perfect agreement between data and model. There are no evident systematic trends in the discrepancies between data and the KMT formalism.

(A color version of this figure is available in the online journal.)

stellar densities in the BR model or high metallicity in the KMT model would imply a high molecular fraction irrespectively of $\Sigma_{\text{H I, obs}}$. If we change perspective for a moment and assume that models are a reliable description of the molecular hydrogen content, the observed trend suggests that low-metallicity galaxies are indeed H I rich. Perhaps, this is not surprising due to the reduced dust content at low metallicity and the consequent reduction of the shielding of molecular gas from the LW-band photons.

4.2.3. Systematic Effects for the KMT Model

Finally, in Figure 7 we explore whether the KMT model exhibits systematic effects within the range of values allowed by the low-resolution sample. For this purpose, we present the ratio $\Sigma_{\text{H I, obs}}/\Sigma_{\text{H I, mod}}$ for the KMT model (red crosses) as a function of the observed metallicity (top panel) and stellar density (bottom panel). As in Figure 6, we display with solid lines the full interval of $\Sigma_{\text{H I, mod}}$. The lack of any evident trend either with metallicity or stellar density suggests that the KMT model is free from systematic effects. In particular, because the four deviant galaxies are not found at systematically high or low metallicity, the difficulties in assessing metallicity for the cold-phase gas could be the cause of such deviations. This hypothesis was touched upon in Section 4.1.1, where we comment on the possibility that metals in the cold gas can in some cases be several factors lower than that observed in the ionized gas. An example of the importance of a correct metallicity determination is provided in Figure 8, where we repeat the comparison between the KMT model and observations in individual galaxies after we arbitrarily redefine $Z' \equiv Z'/3$. As expected, for lower metallicity, the H I saturation moves to higher atomic surface densities and the KMT model better reproduces the observations.

5. DISCUSSION

The analysis presented in Section 4 indicates that extrapolations of the BR model based on pressure overpredict the molecular fraction on small spatial scales (<100 pc), while this formalism recovers the observed values on larger ones. Such a failure of the BR model on small scales was predicted by BR06,

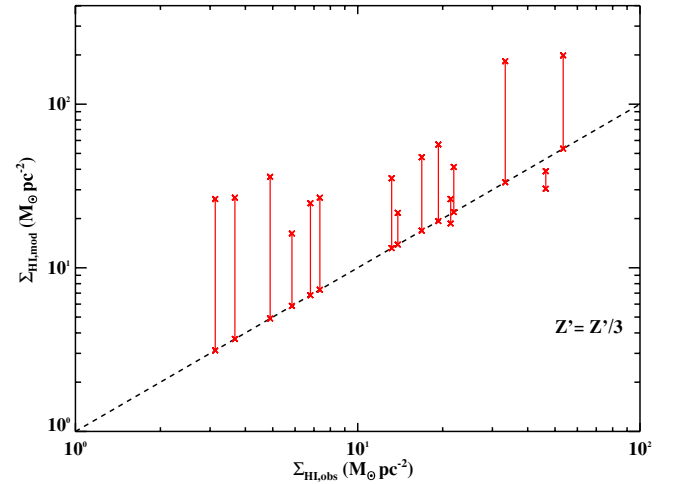


Figure 8. Comparison between the observed H I surface density and the value predicted by the KMT model, as in Figure 6, but for an arbitrarily lower metallicity ($Z' \equiv Z'/3$). A possible cause for the observed discrepancy data model is a lower metallicity in the cold phase than the one observed in the ionized gas.

(A color version of this figure is available in the online journal.)

who point out that the model does not properly account for the effects of gas self-gravity or local variations in the UV radiation field. Conversely, the KMT model based on gas and dust shielding is consistent with most of the observations both locally and on galactic scales, although it is more prone to observational uncertainties in the ISM structure (through the clumping factor) and the cold-phase metallicity. In this section, after a few comments on these points, we will focus on an additional result which emerges from our comparison: the molecular fraction in galaxies depends on the gas column density and metallicity, while it does not respond to local variations in pressure from enhancements in the stellar density.

5.1. The Effect of Self-gravity at Small Scales

The problem of gas self-gravity is that it introduces an additional contribution to the force balance on scales typical for GMCs. In this case, pressure equilibrium with the external ISM is no longer a requirement for local stability and the empirical power law in Equation (7) may break down. However, since self-gravity enhances the internal pressure compared to the ambient pressure in Equation (5), one would expect locally even higher molecular fractions than those predicted by an extrapolation of the BR model. This goes in the opposite direction of our results, since the observed molecular fraction is already overestimated. Hence, a different explanation must be invoked for the data-model discrepancy in Figure 3.

5.2. The Effect of the Radiation Field

A reason for the high $\Sigma_{\text{H I}}$ observed on small spatial scales is related to the intensity of the UV radiation field. In fact, regions which actively form stars probably have an enhanced UV radiation field compared to the mean galactic value. Since the BR formalism does not explicitly contain a dependence on the UV radiation field intensity, it is reasonable to expect discrepancies with observations. In contrast, the KMT model attempts to explicitly account for local variation in j , by considering how such variations affect conditions in the atomic ISM. This makes it more flexible than the BR model in scaling

to environments where conditions vary greatly from those averaged over the entire galaxy.

We stress here that the BR model is not completely independent of the radiation field, but simply does not account for a variation in j . Assuming the scaling relation $f_{\text{H}_2} \sim P^{2.2} j^{-1}$ (Elmegreen 1993), the BR formalism is commonly considered valid only when variations in pressure are much greater than those in j , allowing us to neglect the latter. Being empirically based, the BR model contains information on a mean j , common for nearby spirals. Therefore, this model describes the molecular content as if it were only regulated by pressure.⁷ Hence, it can be applied to describe the molecular fraction only on scales large enough such that variations in the local UV intensity are averaged over many complexes and, eventually, j approaches a mean macroscopic value similar to that found in the galaxies used to fit the BR model.

This idea is quantitatively supported by recent numerical simulations. The molecular fraction of the galaxies simulated by Robertson & Kravtsov (2008) is consistent with the observed $R_{\text{H}_2} \sim P^{0.92}$ only when the effects of the UV radiation field are taken into account. In fact, when neglecting the radiation field, a much shallower dependence $R_{\text{H}_2} \sim P^{0.4}$ is found. In their discussion, the observed power-law index $\alpha \sim 0.9$ results from the combined effects of the hydrostatic pressure and the radiation field. Starting from $f_{\text{H}_2} \propto P^{2.2} j^{-1}$ (Elmegreen 1993), assuming a Kennicutt–Schmidt law in which $j \sim \Sigma_{\text{sfr}} \sim \Sigma_{\text{gas}}^n$, and under the hypothesis that the stellar surface density is related to the gas surface density via a star formation efficiency $\Sigma_{\text{star}} \sim \Sigma_{\text{gas}}^\beta$, $R_{\text{H}_2} = P^\alpha$ requires that (Robertson & Kravtsov 2008)

$$\alpha = 2.2 \frac{(1 + \beta/2) - n}{1 + \beta/2}. \quad (12)$$

In the simulated galaxies, different star formation laws and efficiencies (mostly dependent on the galaxy mass) conspire to reproduce indexes close to the observed $\alpha \sim 0.92$, in support of the idea that a mean value for j is implicitly included in the empirical fit at the basis of the BR model.

5.3. The Effect of Stellar Density

So far, we have discussed why the BR model extrapolated to small spatial scales is unable to predict the observed H I surface density due to its reliance on a fixed “typical” j . Galaxies in our sample are selected to be metal poor, but some of them have a higher SFR (median $\sim 0.6 M_\odot \text{ yr}^{-1}$) and higher specific star formation rate (SSFR; median $\sim 10^{-9} \text{ yr}^{-1}$) than observed in nearby spirals⁸ ($< 10^{-10} \text{ yr}^{-1}$; e.g., Bothwell et al. 2009). If the UV intensity were the only quantity responsible for the disagreement between observations and the BR model below 100 pc, we would also expect some discrepancies on larger scales for galaxies with enhanced star formation. However, such discrepancies are not observed. As discussed, on larger scales, both the KMT and the BR models are able to reproduce observations, despite the different assumptions behind their predictions.

We argue that there is an additional reason for the observed discrepancy between data and the extrapolation of the BR model

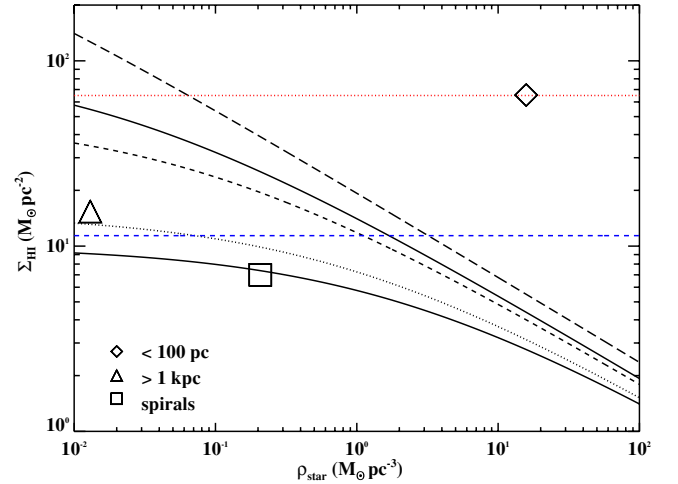


Figure 9. Atomic gas surface density predicted by the BR model (black lines) as a function of the stellar density. Different curves are for different values of the total gas surface density ($\Sigma'_{\text{gas}} = 10$, solid line; $\Sigma'_{\text{gas}} = 15$, dotted line; $\Sigma'_{\text{gas}} = 50$, dashed line; $\Sigma'_{\text{gas}} = 10^2$, dash-dotted line; and $\Sigma'_{\text{gas}} = 10^3$, long-dashed line). The two horizontal lines are for the KMT model at the mean metallicity in the high-resolution sample (red-dotted line) and in the low-resolution sample (blue-dashed line). The open diamond and the open triangle represent the median values of stellar density and H I surface density in the high-resolution and low-resolution samples, respectively. The open square represents a typical stellar density and H I surface density for local spiral galaxies, from a median of the values in Table 1 of BR04, assuming a stellar disk height $h = 300$ pc. Our analysis favors a model in which the molecular fraction in the ISM depends to second order on metallicity rather than stellar density.

(A color version of this figure is available in the online journal.)

below 100 pc. While both models depend to first order on the gas column density, our analysis favors a model in which the local molecular fraction in the ISM depends to second order on metallicity rather than density as in the BR model. To illustrate the arguments in support of this hypothesis, in Figure 9 we show the atomic gas surface density predicted by the BR model (black lines) as a function of the stellar density. Different curves are for different values of the total gas surface density ($\Sigma'_{\text{gas}} = 10$, solid line; $\Sigma'_{\text{gas}} = 15$, dotted line; $\Sigma'_{\text{gas}} = 50$, dashed line; $\Sigma'_{\text{gas}} = 10^2$, dash-dotted line; and $\Sigma'_{\text{gas}} = 10^3$, long-dashed line). Superimposed, there are three data points. The open diamond and the open triangle represent the median values of stellar density and H I surface density for the high-resolution ($\Sigma'_{\text{H I}} = 65$, $\rho'_{\text{star}} = 16$) and low-resolution ($\Sigma'_{\text{H I}} = 15$, $\rho'_{\text{star}} = 0.01$) samples, respectively. The open square represents a typical stellar density and H I surface density ($\Sigma'_{\text{H I}} = 7$, $\rho'_{\text{star}} = 0.2$) for local spiral galaxies, from a median of the values in Table 1 of BR04, assuming a stellar disk height $h = 300$ pc. Finally, the two horizontal lines are for the KMT model at the mean metallicity in the high-resolution sample, $Z' = 0.12$ and in the low-resolution sample, $Z' = 0.20$.

Recalling that for the BR model $P \sim \Sigma_{\text{gas}} v_{\text{gas}} \sqrt{\rho_{\text{star}}}$, we see from Figure 9 that the stellar density does not provide a major contribution to the variation in pressure when $\rho_{\text{star}} \lesssim 0.5$, typical for large galactic regions (open triangle and square). In this regime, the predicted $\Sigma_{\text{H I}}$ from the BR model (black lines) is mostly dependent on variation in the total gas column density alone. In fact, for a constant velocity dispersion, the pressure model becomes equivalent to models based on gas shielding. This reconciles on theoretical grounds the equivalence observed in local spirals between the BR and KMT (blue horizontal

⁷ Incidentally, this exact statement can be found in BR06.

⁸ We recall our choice of the maximum SFR among the values available in the literature to conservatively obtain an upper limit on the molecular emission. For this reason, our median SFR is biased toward high values. In any case, an SFR $\sim 0.3 M_\odot \text{ yr}^{-1}$, typical of BCDs (Hopkins et al. 2002), would correspond to an SSFR $5 \times 10^{-10} \text{ yr}^{-1}$ at the median mass $M_{\text{star}} = 6 \times 10^8 M_\odot$.

dashed line) models. At local scales, i.e., moving toward higher stellar density, ρ_{star} provides an important contribution to the total pressure and the extrapolation of the BR model predicts high molecular gas fractions, as seen in Figure 9. The expected Σ_{HI} drops accordingly, following a trend that is in disagreement with observations (open diamond). Conversely, the KMT model is insensitive to ρ_{star} and accounts only for a variation of the gas column density and metallicity. In this case, the predicted Σ_{HI} (red horizontal dotted line) moves toward higher values in agreement with observations.

From this behavior, we conclude that stellar density is not a relevant quantity in determining the *local* molecular fraction. Furthermore, because the KMT formalism recovers the high observed HI column density for low metallicity, dust and metals have to be important in shaping the molecular content of the ISM. This is further supported by Gnedin & Kravtsov (2010) who show with simulations how the observed SFR, which mostly reflects the molecular gas fraction, depends on the metallicity.⁹ It follows that the observed dependence on the midplane pressure is only an empirical manifestation of the physics which actually regulates the molecular fraction, i.e., the effects of the UV radiation field and the gas and dust shielding.

5.4. Fixed Stellar Density for Molecular Transitions

A final consideration regards the observational evidence that the transition from atomic-to-molecular gas occurs at a fixed stellar density with a small variance among different galaxies (BR04). This result favors hydrostatic pressure models because if the atomic-to-molecular transition were independent of stellar surface density, there would be much more scatter in the stellar surface density than is observed. However, this empirical relation can also be qualitatively explained within a formalism based on UV radiation shielding. In fact, if the bulk of the star formation takes place in molecule-dominated regions, the buildup of the stellar disks eventually will follow the molecular gas distribution, either directly or via a star formation efficiency (see Robertson & Kravtsov 2008; Gnedin & Kravtsov 2010). Since the transition from molecular to atomic hydrogen occurs at a somewhat well-defined gas column density (KMT09; WB02; Bigiel et al. 2008), it is plausible to expect a constant surface stellar density at the transition radius. While this picture would not apply to a scenario in which galaxies grow via subsequent (dry) mergers, recent hydrodynamical simulations (e.g., Brooks et al. 2009) support a model in which stars in disks form from in situ star formation from smoothly accreted cold or shock-heated gas.

6. SUMMARY AND CONCLUSION

With the aim of understanding whether the principal factor that regulates the formation of molecular gas in galaxies is the midplane hydrostatic pressure or shielding from UV radiation by gas and dust, we compared a pressure model (BR model; Wong & Blitz 2002; Blitz & Rosolowsky 2004, 2006) and a model based on UV photodissociation (KMT model; Krumholz et al. 2008, 2009; McKee & Krumholz 2010) against observations of atomic hydrogen and stellar density in nearby metal-poor dwarf galaxies. Due to their low metallicity and high stellar densities, these galaxies are suitable to disentangle the two

models, otherwise degenerate in local spirals because of their proportionality on the gas column density.

Our principal findings can be summarized as follows.

1. On spatial scales below 100 pc, we find that an extrapolation of the BR model (formally applicable above ~ 400 pc) significantly underpredicts the observed atomic gas column densities. Conversely, observations do not disfavor predictions from the KMT model, which correctly reproduces the high HI gas surface densities commonly found at low metallicities.
2. Over larger spatial scales, with the observed and predicted HI surface density integrated over the entire galaxy, we find that both models are able to reproduce observations.
3. Combining our results with numerical simulations of the molecular formation in the galaxies ISM (Elmegreen 1989; Robertson & Kravtsov 2008) which indicates how the UV radiation field (j) plays an essential role in shaping the molecular fraction, we infer that the discrepancy between the BR model and observations on *local scales* is due partially to the model's implicit reliance on an average j , which breaks down at small scales. In contrast, the KMT model properly handles this effect.
4. Since on scales ~ 1 kpc the BR model agrees with observations despite the low metallicity and high specific SFR in our sample, we infer that the discrepancy between pressure models and observations below 100 pc also arises from their dependence on stellar density. An increase in stellar density corresponds to an increase in the hydrostatic pressure which should, in the BR model, reduce the atomic gas fraction. No such trend is seen in the observations.
5. If we drop the dependence on the stellar density, the pressure model reduces to a function of the total gas column density and becomes equivalent to the KMT model, for a fixed velocity dispersion and metallicity. This provides a theoretical explanation for the observed agreement of the two models in local spirals.

In conclusion, our analysis supports the idea that the local molecular fraction is determined by the amount of dust and gas which can shield H_2 from the UV radiation in the LW band. Pressure models are only an empirical manifestation of the ISM properties, with the stellar density not directly related to the H_2 formation. Although they are useful tools to characterize the molecular fraction on large scales, obviating the problem of determining the clumpy structure of the ISM or the metallicity in the cold gas as required by models based on shielding from UV radiation, pressure models should be applied carefully in environments that differ from the ones used in their derivation. These limitations become relevant in simulations and semianalytic models, especially to describe high-redshift galaxies. Furthermore, a correct understanding of the physical processes in the ISM is crucial for the interpretation of observations, an aspect that will become particularly relevant once upcoming facilities such as ALMA will produce high-resolution maps of the ISM at high redshifts.

Combining our analysis with both theoretical and observational efforts aimed at the description of the ISM characteristics and the SFR in galaxies, what emerges is a picture in which macroscopic (hence on galactic scales) properties are regulated by microphysical processes. Specifically, the physics that controls the atomic-to-molecular transition regulates (and is regulated by) the SFR, which sets the UV radiation field intensity. The ongoing star formation is then responsible for increasing the

⁹ However, a detailed analysis of star-forming regions in BCDs by Hirashita & Hunt (2004) suggests that other parameters such as gas density, size, and geometry play a role in determining the local SFR.

ISM metallicity and building new stars, reducing and polluting at the same time the primordial gas content. Without considering violent processes more common in the early universe or in clusters, this chain of events can be responsible for a self-regulated gas consumption and the formation of stellar populations. Future and ongoing surveys of galaxies with low-metallicity, active star formation and high gas fraction (e.g., LITTLE THINGS; Hunter et al.) will soon provide multifrequency observations suitable to test in more detail the progress that has been made on a theoretical basis to understand the process of star formation in galaxies.

We thank Xavier Prochaska, Chris McKee, and Erik Rosolowsky for valuable comments on this manuscript and Robert da Silva for helpful discussions. We thank the referee, Leo Blitz, for his suggestions that helped to improve this work. We acknowledge support from the National Science Foundation through grant AST-0807739 (M.R.K.), from NASA through the Spitzer Space Telescope Theoretical Research Program, provided by a contract issued by the Jet Propulsion Laboratory (M.R.K.), and from the Alfred P. Sloan Foundation (M.R.K.). M.F. is supported by NSF grant (AST-0709235). We acknowledge the usage of the HyperLeda database (<http://leda.univ-lyon1.fr>). This research has made use of the NASA/IPAC Extragalactic Database (NED) which is operated by the Jet Propulsion Laboratory, California Institute of Technology, under contract with the National Aeronautics and Space Administration.

APPENDIX A

NOTES ON INDIVIDUAL GALAXIES

A.1 I Zw 18

The main body of I Zw 18 consists of two main clusters, the northwest (NW) and the southeast (SE) components with an angular separation of $\sim 6''$. A third system, known as “Zwicky’s flare” or “C” component, lies about $22''$ to the NW of the NW cluster. H I maps are available from van Zee et al. (1998b), together with the *HST*/WFPC2 F814W image ($0''.045$ resolution). The H I peaks close to the fainter SE cluster, rather than to the NW where the stellar density is higher. Ly α observations with *HST*/GHRS by Kunth et al. (1994; $2'' \times 2''$ beam) are also available for the NW cloud and have a better resolution than the Very Large Array (VLA) map. At the assumed distance of 13 Mpc (Izotov & Thuan 2004b), $1'' = 63$ pc. Stellar masses of the two massive clusters in I Zw 18 are not published. Hence, multiband integrated photometry of the two star clusters in I Zw 18 is taken from Hunt et al. (2003), together with cluster ages as modeled by them. Sizes of the clusters are measured from fitting Gaussians to the surface brightness profiles (not previously published).

The SE cluster has an age of 10 Myr and, near where the distribution peaks (see van Zee et al. 1998b), $M_K = -12.4$ (in a $2''$ aperture). The lowest-metallicity SB99 models ($Z' = 0.001$) give $M_K = -12.4$, which implies a stellar mass of $2.3 \times 10^5 M_\odot$. With a *K*-band luminosity of $1.91 \times 10^6 L_\odot$, this would give a $(M/L)_K = 0.12$, as inferred from the SB99 models. The Bell & de Jong (2001) predictions give $(M/L)_K = 0.17$, on the basis of $V - K$ and $(M/L)_K = 0.09$, from $V - J$. Hence, the SB99 value of 0.12 is roughly consistent. We therefore adopt the value of $2.3 \times 10^5 M_\odot$ for the stellar mass of the SE cluster. We can check the inferred stellar mass by inspecting the *K*-band surface

brightness at the SE peak (see Figure 5 in Hunt et al. 2003), $\mu_K = 19.2$ mag arcsec $^{-2}$. This gives $\Sigma_K = 185.3 L_\odot \text{pc}^{-2}$ and, assuming $(M/L)_K = 0.12$ from SB99, we would have $\Sigma_{\text{star}} = 22.2 M_\odot \text{pc}^{-2}$. This is in good agreement with the value of $\Sigma_{\text{star}} = 23.3 M_\odot \text{pc}^{-2}$, inferred from the absolute luminosity (see above) and the measured radius of 56 pc.

The NW cluster has an age of 3 Myr and $M_K = -13.25$ (in a $2''$ aperture). The lowest-metallicity SB99 models give $M_K = -16.2$, which is rather uncertain because of the rapid increase in luminosity at about 3 Myr when the most massive stars start evolving off of the main sequence, a phase which is not correctly described in models (Origlia et al. 1999). In fact, the observed $V - H$ color of 0.29 is predicted by SB99 to occur at ~ 10 Myr, not at 3 Myr, which is the best-fit photometric age. In any case, the inferred mass from this model is $6.6 \times 10^4 M_\odot$. With a *K*-band luminosity of $1.91 \times 10^6 L_\odot$, this would give a $(M/L)_K = 0.016$. The same exercise repeated for the *V* band, with $M_V = -12.86$ and the SB99 prediction of $M_V = -15.7$, give an inferred mass of $7.3 \times 10^4 M_\odot$, and $(M/L)_V = 0.006$. These *M/L* values are quite low, roughly six times smaller than those predicted by Bell & de Jong (2001) from the observed colors of I Zw 18. We therefore use the latter *M/L* ratio. With $V - K = 0.38$, $V - H = 0.29$, and $V - I = -0.04$, we estimate $(M/L)_K = 0.11$, 0.10, and 0.09, respectively. Therefore, adopting 0.10, we derive a stellar mass of $4.2 \times 10^5 M_\odot$. Repeating the calculations for *V* band, we find $(M/L)_V = 0.039$, 0.034, and 0.033, respectively. Adopting 0.033, we would derive a similar stellar mass of $3.9 \times 10^5 M_\odot$. Again, the *K*-band surface brightness of the NW cluster ($\mu_K = 18.3$ mag arcsec $^{-2}$, $0''.5$ resolution) gives a similar result. We find $\Sigma_K = 536 L_\odot \text{pc}^{-2}$, and, with $(M/L)_K = 0.10$, becomes $53.6 M_\odot \text{pc}^{-2}$. With a cluster radius of 56 pc ($0''.89$), this would correspond to a cluster mass of $5.3 \times 10^5 M_\odot$, about 1.3 times that inferred from the lower-resolution photometry. Hence, to obviate problems of resolution ($1''$ radius aperture or 63 pc, versus a 56 pc radius measured from the *HST* image), we adopt the mean of these two measurements for the stellar mass of the NW cluster, namely, $4.7 \times 10^5 M_\odot$.

A.2 SBS 0335–052 E

SBS 0335–052 E hosts six SSCs, with most of the star formation activity centered on the two brightest ones to the SE. The H I distribution is published in Ekta et al. (2009), and the *HST*/ACS F555M image ($0''.050$ resolution), was published by Reines et al. (2008). The H I map is of relatively low resolution ($\sim 3''.4$) and does not resolve the six SSCs individually since they are distributed (end to end) over roughly $2''.6$. Ly α observations with *HST*/GHRS by Thuan & Izotov (1997; $2'' \times 2''$ beam) are also available. In our analysis, we use this column density, being at better resolution than the one derived from H I emission map. At the assumed distance of 53.7 Mpc, $1'' = 260.3$ pc. Stellar masses for individual clusters have been derived by Reines et al. (2008) by fitting the optical and UV spectral energy distributions, and we adopt these masses here. Comparison with masses inferred from *K* band is unfruitful since nebular and ionized gas contamination make this estimate highly uncertain. We measure the size of the clusters by fitting two-dimensional Gaussians. They are unresolved at the *HST*/ACS resolution of $0''.050$, but since they have the same size to within 13%, we assume the average radius of 18.2 pc. Therefore, the inferred mass densities result in lower limits.

A.3 Mrk 71

A.4 UM 462

Mrk 71 (NGC 2363) is a complex of H II regions in a larger irregular galaxy, NGC 2366. There are two main knots of star formation activity (see Drissen et al. 2000), denoted A and B. A low-resolution H I map ($12''.5 \times 11''.5$) is available from Thuan et al. (2004), but at this resolution we are unable to distinguish the two main clusters which are $5''$ apart. At the assumed distance of 3.44 Mpc (derived from Cepheids; Tolstoy et al. 1995), $1'' = 16.7$ pc. Stellar masses of the two starburst knots in Mrk 71 are not published. Hence, V -band photometry was taken from Drissen et al. (2000), and I band from Thuan & Izotov (2005), together with cluster ages as modeled by Drissen et al. (2000). As for I Zw 18, sizes of the clusters were measured from fitting one-dimensional Gaussians to the surface brightness profiles.

The knot A has $V = 17.3$ mag and, after correcting for $A_V = 0.3$ mag, we derive an absolute magnitude $M_V = -10.4$. At an age of 3 Myr, SB99 models (at $Z = 0.004$) predict $M_V = -15.2$. We would thus infer a stellar mass of $1.2 \times 10^4 M_\odot$ and an implied $(M/L)_V$ ratio of 0.012. The Bell & de Jong (2001) predictions give $(M/L)_V = 0.010$, on the basis of stellar $V - K = -0.42$, as modeled by Noeske et al. (2000), and $(M/L)_V = 0.10$, from stellar $B - V = -0.19$ (also as in Noeske et al. 2000). The latter value from $B - V$ is a factor of 10 higher than the former from $V - K$, and highly inconsistent with the SB99 value of 0.01. The I -band photometry of knot A from Thuan & Izotov (2005) gives a similar inconsistency. With $I = 17.97$ mag, and a corresponding absolute magnitude of 9.71, we would infer a stellar luminosity of $3.43 \times 10^5 L_\odot$. With Bell & de Jong (2001) $(M/L)_I$ values of 0.025 (from $V - K$) and 0.15 (from $B - V$), we would derive stellar masses of 8.6×10^3 and $5.1 \times 10^4 M_\odot$, respectively. Since three values are roughly consistent ($\sim 10^4 M_\odot$), we adopt $1.2 \times 10^4 M_\odot$ as the mass for knot A.

Knot B is slightly older than knot A (4 Myr) consistent with its Wolf-Rayet stars and strong stellar winds as inferred from P Cygni like profiles in the UV (Drissen et al. 2000). It is also slightly fainter with $V = 18.05$ (after correcting for $A_V = 0.3$ mag), corresponding to an absolute magnitude $M_V = -9.63$. SB99 models (at 4 Myr) predict $M_V = -15.3$, which would give a stellar mass of $5.4 \times 10^3 M_\odot$, and an implied $(M/L)_V$ ratio of 0.005. Again, we derive M/L ratios as a function of color from Bell & de Jong (2001), and obtain $(M/L)_V = 0.06$ from stellar $V - K = 0.67$ and $(M/L)_V = 0.15$, from stellar $B - V = -0.07$ (Noeske et al. 2000). With a stellar V -band luminosity of $6.1 \times 10^5 L_\odot$, we would infer a stellar mass of $3.6 \times 10^4 M_\odot$ with $(M/L)_V = 0.06$, and $9.2 \times 10^4 M_\odot$ with $(M/L)_V = 0.15$. Both masses are larger than those inferred for knot A, inconsistently with the observation of Drissen et al. (2000) that knot B contains only $\sim 6\%$ of the ionizing photons necessary to power the entire H II region. Nevertheless, knot A is supposedly enshrouded in dust (Drissen et al. 2000), so the situation is unclear. The I -band photometry of knot B from Thuan & Izotov (2005) is not edifying. With $I = 18.92$ mag, and a corresponding absolute magnitude of -8.76 , we would infer a stellar luminosity of $1.43 \times 10^5 L_\odot$. With Bell & de Jong (2001) $(M/L)_I$ values of 0.10 (from $V - K$) and 0.20 (from $B - V$), we would derive stellar masses of $1.4 \times 10^4 M_\odot$ and $2.9 \times 10^4 M_\odot$, respectively. These values are all greater than the mass inferred for knot A, even though knot B is reputed to be intrinsically ~ 16 times fainter (see above, and Drissen et al. 2000). For this reason, we adopt the SB99 value of $5.4 \times 10^3 M_\odot$ as the mass for knot B.

UM 462 hosts six SSCs, with $9''$ separation from end to end. The H I distribution is available in the literature from van Zee et al. (1998a), together with the ground-based ESO/SOFI K_s image ($0''.28$ pixels, $0''.8$ – $1''$ seeing) from Vanzi (2003). The resolution of the H I map ($6''.6 \times 5''.2$) is just barely sufficient to distinguish the two clusters. At the assumed distance of 13.5 Mpc, $1'' = 65.4$ pc. Stellar masses of the six SSCs in UM 462 have been derived by Vanzi (2003) by estimating the age from the H α equivalent width, then comparing SB99 models at that age with the H α luminosity of the cluster after correcting for extinction. These estimates differ from the other SB99 comparisons described for previous galaxies because they extend to a lower lower-mass limit, $0.1 M_\odot$ rather than $1 M_\odot$. We thus consider a range of possible masses given by the values published by Vanzi (2003) and what we infer from comparing the K_s -band luminosities of the individual clusters with SB99 predictions as above (at the published age). On the basis of the observed $V - K_s$ and $V - J$ colors (Vanzi et al. 2002; Vanzi 2003), we derive $(M/L)_K = 0.05$ according to Bell & de Jong (2001). A comparison of these numbers with the values provided by Vanzi (2003) reveals that typical uncertainty on the mass calculations are roughly a factor of 2 or less. Sizes are measured by Vanzi et al. (2002), but the clusters are unresolved at the ground-based resolution. Hence, the mass densities are formally lower limits.

A.5 II Zw 40

II Zw 40 is a cometary BCD with two tails. The main star formation activity is occurring at the “head of the comet,” namely, in two knots in a north–south orientation, separated vertically by $1''.5$. The upper knot, dubbed “A” by Vanzi et al. (2008), is elongated along roughly an east–west direction and contains the rising-spectrum thermal radio sources found by Beck et al. (2002). The lower B knot is round, fainter than A, and apparently does not host any compact radio sources. The H I distribution is published in van Zee et al. (1998a) and *HST*/F814W images ($0''.025$ pixels) are also available. The resolution of the H I map, $5''.7 \times 4''.8$, does not distinguish the two knots seen at *HST* resolution. At the assumed distance of 10.3 Mpc, $1'' = 49.9$ pc. II Zw 40 is located sufficiently near the plane of the Milky Way that the foreground extinction is quite high, $A_V = 2.7$ mag. Stellar masses of the two clusters in II Zw 40 have been derived by Vanzi et al. (2008), but with a Kroupa IMF and using Br γ luminosity (see also UM 462) in a $15''$ aperture. Moreover, a subtraction procedure was applied that made assumptions about the Br γ flux of region A in the vicinity of knot B. Hence, to test these values for stellar masses, we recompute them from continuum measurements, using similar procedures to those used for the previous galaxies.

Ages for the clusters are taken from Vanzi et al. (2008), who compared observed Br γ equivalent widths to SB99 model predictions. Photometry in the *HST* F555W, F814W, and F160W passbands is performed by fitting a two-dimensional Gaussian to each knot. This determination is roughly consistent with aperture photometry in a $1''$ aperture. Correcting the observed magnitudes for the high extinction as in Vanzi et al. (2008) from the NIR hydrogen recombination lines ($A_V = 4.0$ mag for knot A, $A_V = 4.9$ mag for knot B), we have 14.62, 15.80, and 13.34 for F555W, F814W, and F160W, respectively (knot A), and 14.13, 14.58, and 13.31 for F555W, F814W, and F160W (knot B). Under the approximation $F555W \sim V$, we derive an

absolute magnitude of -15.4 for knot A, to be compared with the SB99 prediction of -15.2 (at 3 Myr), and -15.9 for knot B to be compared with -15.5 (at 7 Myr). The comparisons with SB99 give stellar masses of $1.2 \times 10^6 M_{\odot}$ and $1.5 \times 10^6 M_{\odot}$, for knots A and B, respectively (the inferred $(M/L)_{\nu}$ are 0.01 and 0.007 for knots A and B). With the approximation $F555W \sim V$, $F814W \sim I$, and $F160W \sim H$, $V - I = -1.18$ and -0.45 , and $V - H = 1.31$ and 0.82 for knots A and B, respectively. Using Bell & de Jong (2001), we derive $(M/L)_{\nu} = 0.0005$ and 0.004 from $V - I$, and $(M/L)_{\nu} = 0.21$ and 0.09 from $V - H$.

These values differ substantially from those inferred from SB99. In particular, the value of 0.0005 is unrealistic, and difficult to reconcile with other galaxies and other M/L inferred for II Zw 40. Hence, we consider a range of stellar masses for knot A with $6.4 \times 10^5 M_{\odot}$ (for $(M/L)_{\nu} = 0.005$) and $1.2 \times 10^6 M_{\odot}$ (SB99) as lower and upper limits. For knot B instead, we assume a lower limit at $8.1 \times 10^5 M_{\odot}$ (for $(M/L)_{\nu} = 0.004$) and an upper limit at $1.5 \times 10^6 M_{\odot}$ (SB99). These are roughly consistent with the masses given by Vanzi et al. (2008) of $1.7 \times 10^6 M_{\odot}$ for knot A and $1.3 \times 10^5 M_{\odot}$ for knot B, as inferred from comparing SB99 predictions of $\text{Br}\gamma$ emission over a $15''$ aperture (knot A) and $0''.75$ aperture (knot B). For the sizes of the two clusters, we fit a one-dimensional Gaussian to the surface brightness profiles in the F814W band and obtain 10.1 pc for knot A and 5.2 pc for knot B. The dimensions derived by fitting two-dimensional Gaussians are smaller, namely, 4.4 pc (A) and 3.7 pc (B), similar to the dimensions obtained by Vanzi et al. (2008) for the star cluster itself (rather than the more extended H II region emission).

A.6 NGC 5253

NGC 5253 is a nearby dwarf galaxy in the Centaurus group at a distance of 3.5 Mpc. Its morphology is peculiar; the outer isophotes resemble a dwarf elliptical, but over time NGC 5253 has been classified as a spiral, an elliptical, an S0, an irregular, and most recently, as an amorphous galaxy (Caldwell & Phillips 1989). A blue starburst dominates the central region, with a dust lane bisecting the main body along the minor axis. The central starburst comprises at least six SSCs, identified by Calzetti et al. (1997), who published *HST* multiband *HST*/WFPC2 images of the galaxy with a resolution of $0''.1$. The H I distribution is published by Kobulnicky & Skillman (2008), with a beam size of $9''.0 \times 7''.6$.

Calzetti et al. (1997) have measured the cluster ages by comparing colors and equivalent width of hydrogen recombination lines with SB99 predictions. The reddest cluster, NGC 5253-5, has an age of $\lesssim 2.5$ Myr, and dominates the infrared spectral energy distribution (Vanzi & Sauvage 2004); its visual extinction A_V is uncertain but could be as large as 35 mag (Calzetti et al. 1997), although is probably around 7–8 mag (Vanzi & Sauvage 2004). The brightest and bluest cluster, NGC 5253-4, is also quite young, ~ 2.5 Myr, but the remaining SSCs are older, ~ 10 –50 Myr. Stellar masses of the SSCs have been inferred by Calzetti et al. (1997) and Vanzi & Sauvage (2004), through comparison of the observed broadband luminosities to SB99 predictions, given the age of the cluster. Masses range from $\sim 10^4 M_{\odot}$ (NGC 5253-4) to $10^6 M_{\odot}$ (NGC 5253-5), and radii from 1.6 to 3.5 pc, as measured from *HST* images.

A.7 NGC 1140

NGC 1140 is an amorphous, irregular galaxy, and, like NGC 5253, has been reclassified over the course of time (Hunter et al. 1994a). Optically, it is dominated by a supergiant H II

region encompassing $\sim 10^4$ OB stars, far exceeding the stellar content of the giant H II region, 30 Doradus, in the LMC (Hunter et al. 1994a). The H II region is powered by several SSCs (Hunter et al. 1994a; de Grijs et al. 2004), situated in a vertical strip, about $10''$ in length. High-resolution *HST*/WFPC2 images exist for this galaxy (Hunter et al. 1994a), and H I maps have been published by Hunter et al. (1994b). The resolution of the H I map ($16'' \times 22''$) is insufficient to distinguish the clusters; given this resolution, the peak $\Sigma_{\text{H I}}$ is certainly underestimated.

Stellar masses have been determined for the SSCs in NGC 1140 by de Grijs et al. (2004), using a minimization technique which simultaneously estimates stellar ages and masses, metallicities, and extinction using broadband fluxes. We prefer these masses to those measured by a virial technique (Moll et al. 2009), as the latter can be an order of magnitude larger, perhaps due to non-virial line widths. Sizes were measured by Moll et al. (2009) for the brightest clusters 1 and 6, and we have used these, after correcting for the different distance scale.

APPENDIX B

STELLAR MASSES FOR THE LOW-RESOLUTION SAMPLE

To compute stellar masses for the low-resolution sample of 16 objects, we acquired IRAC 3.6 and 4.5 μm data from the *Spitzer* archive for all galaxies in the sample (3.6 μm images are unavailable for two objects). Starting from the Basic Calibrated Data, we co-add frames using MOPEX, the image mosaicing and source-extraction package provided by the Spitzer Science center (Makovoz & Marleau 2005). Pixels flagged by masks are ignored. Additional inconsistent pixel values are removed by means of the MOPEX outlier rejection algorithms, in particular the dual-outlier technique, together with the multiframe algorithm. We correct the frames for geometrical distortion and then project them onto a fiducial coordinate system with pixel sizes of $1''.2$, roughly equivalent to the original pixels. Standard linear interpolation is used for the mosaics. The noise levels in our MOPEX IRAC mosaics are comparable to or lower than those in the pipeline products. We then perform aperture photometry on the IRAC images with the IRAF photometry package *apphot* and applying appropriate unit conversion to compute integrated fluxes. The background level is determined by averaging several adjacent empty sky regions. Fluxes are computed with a curve-of-growth analysis at radii where the growth curve becomes asymptotically flat. From this analysis, we determined the half-light (effective) diameter and the size of the object as the point at which the growth curve achieves flatness. Our values for IRAC sizes are on average 1.24 times the geometric means of the optical dimensions (as reported in NED). Although the standard deviation is large (0.48), this could indicate that there is an evolved stellar population in the extended regions of the galaxies that is not seen at optical wavelengths. Alternatively, it could merely be an effect of surface brightness since the optical diameters are isophotal and, for a given optical surface brightness, the IR images could be deeper. In addition, the two methods of measuring sizes also differ (isophotal in the optical, and photometric in the IR). In fact, the approximation of a circular virtual aperture could contribute to the larger sizes measured with IRAC.

From the IRAC photometry, we derive stellar masses following Lee et al. (2006) by inferring *K*-band luminosities from IRAC [4.5] total magnitudes (with a color correction), and a color-dependent ($B - K$) mass-to-light ratio. To increase the

Table 3
Photometric Quantities for the Low-resolution Sample^a

Name	<i>B</i> (mag)	<i>K</i> (mag)	<i>K</i> ([3.6]) ^b (mag)	<i>K</i> ([4.5]) ^c (mag)	<i>B</i> − <i>K</i> (Min.) (mag)	<i>B</i> − <i>K</i> (Mean) (mag)	<i>B</i> − <i>K</i> (Std) (mag)	<i>M</i> _{star,K} (Min.) (<i>M</i> _⊙)	<i>M</i> _{star,K} (Avg) (<i>M</i> _⊙)
Haro3	13.22	10.61	...	10.05	2.61	2.89	0.40	9.09	9.35
IIZw 40	11.94	10.98	10.89	10.22	0.96	1.24	0.42	8.09	8.34
IZw 18	15.86	15.24	14.59	14.45	0.62	1.10	0.42	6.51	6.88
Mrk 209	15.09	12.50	...	12.68	2.40	2.49	0.12	7.29	7.36
Mrk 33	13.39	10.42	10.09	10.13	2.96	3.17	0.18	9.59	9.79
Mrk 71	11.44	...	11.74	10.90	−0.30	0.12	0.60	6.54	6.89
NGC 1140	13.46	10.48	9.92	10.07	2.98	3.30	0.29	9.30	9.58
NGC 1156	11.35	9.45	8.49	8.51	1.90	2.53	0.55	8.62	9.10
NGC 1741	13.08	11.82	10.76	10.78	1.26	1.96	0.61	9.29	9.81
NGC 2537	12.09	9.11	8.91	9.02	2.98	3.07	0.10	9.14	9.26
NGC 4214	10.15	7.90	7.92	...	2.22	2.23	0.02	8.66	8.67
NGC 5253	10.63	8.21	7.60	7.23	2.41	2.95	0.50	8.63	9.05
NGC 7077	13.90	11.36	11.39	11.47	2.42	2.49	0.06	8.54	8.60
SBS 0335 − 052	16.45	15.40	14.02	12.79	1.05	2.38	1.31	7.79	8.72
UM 448	14.44	11.33	10.65	10.49	3.11	3.62	0.45	10.30	10.69
UM 462	14.42	12.70	12.33	12.20	1.72	2.01	0.26	7.95	8.20

Notes.

^a See Appendix B for a detailed description of the listed quantities.

^b Assumed $K - [3.6] = 0.03$.

^c Assumed $K - [4.5] = 0.20$.

reliability of this procedure, we include and calibrate with a similar procedure the IRAC [3.6] magnitudes, and, where available, also incorporate *K*-band magnitudes from Two Micron All Sky Survey (2MASS). The average of these three values (one *K* band, and two indirect *K*-band estimates) are used to calculate the $B - K$ color for the M/L ratio, and the *K*-band luminosity. These magnitudes and colors are reported in Table 3.

As previously mentioned, inferring stellar masses photometrically can be problematic for some of the BCDs in our sample. Hot dust, together with free-free nebular continuum or a high equivalent-width $\text{Br}\alpha$ line, can contaminate the broadband fluxes from 2 to 5 μm (Hunt et al. 2002; Smith & Hancock 2009). For this reason *K*, [3.6], and [4.5] magnitudes can potentially be poor indicators of stellar mass. An extreme case is SBS 0335−052 E, one of the lowest-metallicity objects in the sample, where 50% of the *K*-band emission is gas, and 13% is dust. Only 37% of the 2 μm emission is stellar (Hunt et al. 2001). At 3.8 μm (ground-based *L* band), the situation is even worse, with stars comprising only 6% of the emission. Hence, to mitigate the potential overestimate of the stellar mass from contaminated red colors, the minimum (bluest) colors were used to infer the mass-to-light ratio (because of its $B - K$ dependence), and the *K*-band luminosity. A comparison between the mass-metallicity relation obtained with our inferred stellar masses and the sample in Lee et al. (2006) suggests that the use of the minimum stellar masses (bluest colors) is strongly advocated (with an error of a factor 2–3).

APPENDIX C

CONSTRAINTS ON THE TOTAL GAS COLUMN DENSITY

The analysis presented in the main text is entirely based on lower limits on the total gas surface density, because of the impossibility to reliably establish the H_2 abundances from the available CO observations. However, we can impose conservative upper limits on Σ_{gas} using indirect ways to quantify Σ_{H_2} .

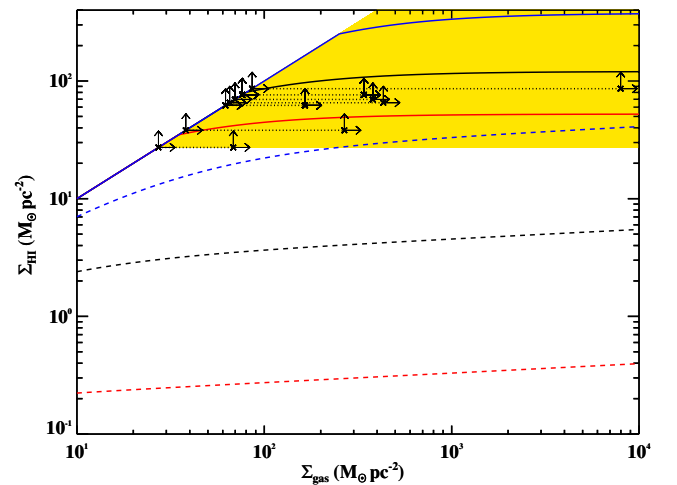


Figure 10. Same as Figure 4, but with conservative estimates for the total gas column density inferred from SFRs.

(A color version of this figure is available in the online journal.)

For the high-resolution sample, we derive Σ_{gas} from the molecular gas column density as inferred by means of the SFRs, assuming a depletion time $t_{\text{depl}} \sim 2$ Gyr (Bigiel et al. 2008) for molecular gas. Formally, this should correspond to an upper limit on Σ_{H_2} , mainly because we use SFRs integrated on scales which are much greater than the individual associations we are studying. However, since the H I surface density is not precisely known, we cannot regard Σ_{gas} as real upper limits, although we argue that they likely are. Using these limits, we can explicitly show that the disagreement between the extrapolation of the BR model and the observations presented in the Section 4.1.3 cannot simply be explained with high gas column densities. This is shown in Figure 10, where we present once again both the models and data, adding conservative estimates for Σ_{gas} , connected with a dotted line. The fact that the derived $\Sigma'_{\text{gas}} \sim (2-3) \times 10^3$ are not enough to account for the observed

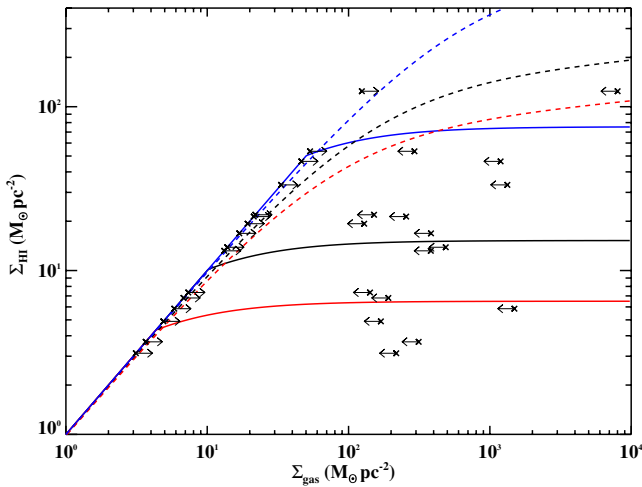


Figure 11. Same as Figure 5, but with upper limits on the total gas surface density inferred from either CO fluxes or SFRs.

(A color version of this figure is available in the online journal.)

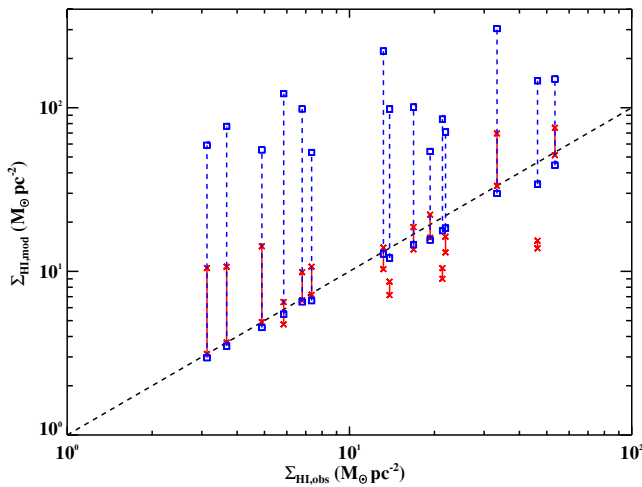


Figure 12. Same as Figure 6, but with lines to connect lower and upper limits on $\Sigma_{\text{H}_2, \text{mod}}$ for the BR model. Upper limits on $\Sigma_{\text{H}_2, \text{mod}}$ are derived assuming an upper limit on Σ_{gas} .

(A color version of this figure is available in the online journal.)

discrepancy confirm the results inferred using lower limits only (Figure 4).

Similarly, for the low-resolution sample, we set conservative upper limits on Σ_{gas} assuming a CO-to-H₂ conversion factor $X = 11 \times 10^{21} \text{ cm}^{-2} \text{ K}^{-1} \text{ km}^{-1} \text{ s}$ (Leroy et al. 2009). Being derived from one of the highest X published to date, the inferred Σ_{H_2} are likely to be truly upper limits on the intrinsic H₂. However, whenever these are smaller than Σ_{H_2} as obtained from the SFRs combined with a depletion time $t_{\text{depl}} \sim 2 \text{ Gyr}$, we assume conservatively the latter values. This may be warranted since some galaxies in our sample are at even lower metallicity than the one assumed in CO-to-H₂ conversion factor used here. These upper limits on Σ_{H_2} are shown in Figure 11 and can be used in turn to set upper limits on $\Sigma_{\text{H}_2, \text{mod}}$ for the BR model (see Figure 6 and Section 4.2.2), as in Figure 12. Because these upper limits on $\Sigma_{\text{H}_2, \text{mod}}$ exceed significantly the model expectations at low metallicity, we infer that some caution is advisable when extrapolating local empirical star formation laws to high redshift, in dwarf galaxies or in the outskirts of spiral galaxies (see Fumagalli & Gavazzi 2008).

REFERENCES

- Albrecht, M., Chini, R., Krügel, E., Müller, S. A. H., & Lemke, R. 2004, *A&A*, **414**, 141
- Asplund, M., Grevesse, N., Sauval, A. J., & Scott, P. 2009, *ARA&A*, **47**, 481
- Barone, L. T., Heithausen, A., Hüttemeister, S., Fritz, T., & Klein, U. 2000, *MNRAS*, **317**, 649
- Beck, S. C., Turner, J. L., Langland-Shula, L. E., Meier, D. S., Crosthwaite, L. P., & Gorjian, V. 2002, *AJ*, **124**, 2516
- Bell, E. F., & de Jong, R. S. 2001, *ApJ*, **550**, 212
- Bell, E. F., McIntosh, D. H., Katz, N., & Weinberg, M. D. 2003, *ApJS*, **149**, 289
- Bigiel, F., Leroy, A., Walter, F., Brinks, E., de Blok, W. J. G., Madore, B., & Thornley, M. D. 2008, *AJ*, **136**, 2846
- Blitz, L., & Rosolowsky, E. 2004, *ApJ*, **612**, L29
- Blitz, L., & Rosolowsky, E. 2006, *ApJ*, **650**, 933
- Bolatto, A. D., Leroy, A. K., Rosolowsky, E., Walter, F., & Blitz, L. 2008, *ApJ*, **686**, 948
- Boselli, A., & Gavazzi, G. 2006, *PASP*, **118**, 517
- Bothwell, M. S., Kennicutt, R. C., & Lee, J. C. 2009, *MNRAS*, **400**, 154
- Bowen, D. V., Jenkins, E. B., Pettini, M., & Tripp, T. M. 2005, *ApJ*, **635**, 880
- Brooks, A. M., Governato, F., Quinn, T., Brook, C. B., & Wadsley, J. 2009, *ApJ*, **694**, 396
- Caldwell, N., & Phillips, M. M. 1989, *ApJ*, **338**, 789
- Calzetti, D., Meurer, G. R., Bohlin, R. C., Garnett, D. R., Kinney, A. L., Leitherer, C., & Storchi-Bergmann, T. 1997, *AJ*, **114**, 1834
- Campos-Aguilar, A., Moles, M., & Masegosa, J. 1993, *AJ*, **106**, 1784
- Chung, A., van Gorkom, J. H., Kenney, J. D. P., Crowl, H., & Vollmer, B. 2009, *AJ*, **138**, 1741
- Dale, D. A., Helou, G., Neugebauer, G., Soifer, B. T., Frayer, D. T., & Condon, J. J. 2001, *AJ*, **122**, 1736
- Davidge, T. J. 1989, *PASP*, **101**, 494
- de Grijs, R., et al. 2004, *MNRAS*, **352**, 263
- de Vaucouleurs, G., de Vaucouleurs, A., Corwin, H. G., Jr., Buta, R. J., Paturel, G., & Fouque, P. 1991, Third Reference Catalog of Bright Galaxies, Vols. 1–3, XII (Berlin: Springer)
- Drissen, L., Roy, J.-R., Robert, C., Devost, D., & Doyon, R. 2000, *AJ*, **119**, 688
- Ekta, B., Pustilnik, S. A., & Chengalur, J. N. 2009, *MNRAS*, **397**, 963
- Elmegreen, B. G. 1989, *ApJ*, **338**, 178
- Elmegreen, B. G. 1993, *ApJ*, **411**, 170
- Fumagalli, M., & Gavazzi, G. 2008, *A&A*, **490**, 571
- Fumagalli, M., Krumholz, M. R., Prochaska, J. X., Gavazzi, G., & Boselli, A. 2009, *ApJ*, **697**, 1811
- Gil de Paz, A., Silich, S. A., Madore, B. F., Sánchez Contreras, C., Zamorano, J., & Gallego, J. 2002, *ApJ*, **573**, L101
- Gnedin, N. Y., & Kravtsov, A. V. 2010, *ApJ*, **714**, 287
- Gnedin, N. Y., Tassis, K., & Kravtsov, A. V. 2009, *ApJ*, **697**, 55
- Hirashita, H., & Hunt, L. K. 2004, *A&A*, **421**, 555
- Hopkins, P. F., Murray, N., Quataert, E., & Thompson, T. A. 2010, *MNRAS*, **401**, L19
- Hopkins, A. M., Schulte-Ladbeck, R. E., & Drozdovsky, I. O. 2002, *AJ*, **124**, 862
- Hunt, L., Bianchi, S., & Maiolino, R. 2005a, *A&A*, **434**, 849
- Hunt, L. K., Dyer, K. K., & Thuan, T. X. 2005b, *A&A*, **436**, 837
- Hunt, L. K., Dyer, K. K., Thuan, T. X., & Ulvestad, J. S. 2004, *ApJ*, **606**, 853
- Hunt, L. K., Giovanardi, C., & Helou, G. 2002, *A&A*, **394**, 873
- Hunt, L. K., Thuan, T. X., & Izotov, Y. I. 2003, *ApJ*, **588**, 281
- Hunt, L. K., Vanzil, L., & Thuan, T. X. 2001, *A&A*, **377**, 66
- Hunter, D. A., O’Connell, R. W., & Gallagher, J. S., III. 1994a, *AJ*, **108**, 84
- Hunter, D. A., van Woerden, H., & Gallagher, J. S., III. 1994b, *ApJS*, **91**, 79
- Imara, N., & Blitz, L. 2007, *ApJ*, **662**, 969
- Izotov, Y. I., & Thuan, T. X. 2004a, *ApJ*, **602**, 200
- Izotov, Y. I., & Thuan, T. X. 2004b, *ApJ*, **616**, 768
- Izotov, Y. I., Thuan, T. X., & Lipovetsky, V. A. 1997, *ApJS*, **108**, 1
- Kennicutt, R. C., Jr. 1998, *ARA&A*, **36**, 189
- Kennicutt, R. C., Jr., et al. 2007, *ApJ*, **671**, 333
- Kobulnicky, H. A., & Skillman, E. D. 2008, *AJ*, **135**, 527
- Krumholz, M. R., McKee, C. F., & Tumlinson, J. 2008, *ApJ*, **689**, 865
- Krumholz, M. R., McKee, C. F., & Tumlinson, J. 2009, *ApJ*, **693**, 216
- Kunth, D., Lequeux, J., Sargent, W. L. W., & Viallefond, F. 1994, *A&A*, **282**, 709
- Lebouteiller, V., Kunth, D., Lequeux, J., Lecavelier des Etangs, A., Désert, J.-M., Hébrard, G., & Vidal-Madjar, A. 2004, *A&A*, **415**, 55
- Lebouteiller, V., Kunth, D., Thuan, T. X., & Désert, J. M. 2009, *A&A*, **494**, 915
- Lecavelier des Etangs, A., Désert, J.-M., Kunth, D., Vidal-Madjar, A., Callejo, G., Ferlet, R., Hébrard, G., & Lebouteiller, V. 2004, *A&A*, **413**, 131
- Lee, J. C., Salzer, J. J., Impy, C., Thuan, T. X., & Gronwall, C. 2002, *AJ*, **124**, 3088

- Lee, H., Skillman, E. D., Cannon, J. M., Jackson, D. C., Gehrz, R. D., Polomski, E. F., & Woodward, C. E. 2006, *ApJ*, **647**, 970
- Leitherer, C., et al. 1999, *ApJS*, **123**, 3
- Leon, S., Combes, F., & Menon, T. K. 1998, *A&A*, **330**, 37
- Leroy, A., Bolatto, A. D., Simon, J. D., & Blitz, L. 2005, *ApJ*, **625**, 763
- Leroy, A., Cannon, J., Walter, F., Bolatto, A., & Weiss, A. 2007, *ApJ*, **663**, 990
- Leroy, A. K., Walter, F., Brinks, E., Bigiel, F., de Blok, W. J. G., Madore, B., & Thornley, M. D. 2008, *AJ*, **136**, 2782
- Leroy, A. K., et al. 2009, *ApJ*, **702**, 352
- Makovoz, D., & Marleau, F. R. 2005, *PASP*, **117**, 1113
- McKee, C. F., & Krumholz, M. R. 2010, *ApJ*, **709**, 308
- Meurer, G. R., Heckman, T. M., Leitherer, C., Kinney, A., Robert, C., & Garnett, D. R. 1995, *AJ*, **110**, 2665
- Moll, S. L., de Grijs, R., Mengel, S., Smith, L. J., & Crowther, P. A. 2009, *Ap&SS*, **324**, 177
- Murante, G., Monaco, P., Giovalli, M., Borgani, S., & Diaferio, A. 2010, *MNRAS*, **405**, 1491
- Narayanan, D., Hayward, C. C., Cox, T. J., Hernquist, L., Jonsson, P., Younger, J. D., & Groves, B. 2010, *MNRAS*, **401**, 1613
- Noeske, K. G., Guseva, N. G., Fricke, K. J., Izotov, Y. I., Papaderos, P., & Thuan, T. X. 2000, *A&A*, **361**, 33
- O'Connell, R. W., Gallagher, J. S., III, & Hunter, D. A. 1994, *ApJ*, **433**, 65
- Origlia, L., Goldader, J. D., Leitherer, C., Schaerer, D., & Oliva, E. 1999, *ApJ*, **514**, 96
- Paturel, G., Petit, C., Prugniel, P., Theureau, G., Rousseau, J., Brouty, M., Dubois, P., & Cambr esy, L. 2003, *A&A*, **412**, 45
- Pelupessy, F. I., Papadopoulos, P. P., & van der Werf, P. 2006, *ApJ*, **645**, 1024
- Pustilnik, S. A., Brinks, E., Thuan, T. X., Lipovetsky, V. A., & Izotov, Y. I. 2001, *AJ*, **121**, 1413
- Reines, A. E., Johnson, K. E., & Hunt, L. K. 2008, *AJ*, **136**, 1415
- Robertson, B. E., & Kravtsov, A. V. 2008, *ApJ*, **680**, 1083
- Sage, L. J., Salzer, J. J., Loose, H.-H., & Henkel, C. 1992, *A&A*, **265**, 19
- Schmitt, H. R., Calzetti, D., Armus, L., Giavalisco, M., Heckman, T. M., Kennicutt, R. C., Jr., Leitherer, C., & Meurer, G. R. 2006, *ApJS*, **164**, 52
- Smith, B. J., & Hancock, M. 2009, *AJ*, **138**, 130
- Taylor, C. L., Koblunicky, H. A., & Skillman, E. D. 1998, *AJ*, **116**, 2746
- Thuan, T. X., Hibbard, J. E., & L evrier, F. 2004, *AJ*, **128**, 617
- Thuan, T. X., & Izotov, Y. I. 1997, *ApJ*, **489**, 623
- Thuan, T. X., & Izotov, Y. I. 2005, *ApJ*, **627**, 739
- Thuan, T. X., Lecavelier des Etangs, A., & Izotov, Y. I. 2005, *ApJ*, **621**, 269
- Tolstoy, E., Saha, A., Hoessel, J. G., & McQuade, K. 1995, *AJ*, **110**, 1640
- van Dishoeck, E. F., & Black, J. H. 1986, *ApJS*, **62**, 109
- van Zee, L., & Haynes, M. P. 2006, *ApJ*, **636**, 214
- van Zee, L., Skillman, E. D., & Salzer, J. J. 1998a, *AJ*, **116**, 1186
- van Zee, L., Westpfahl, D., Haynes, M. P., & Salzer, J. J. 1998b, *AJ*, **115**, 1000
- Vanzi, L. 2003, *A&A*, **408**, 523
- Vanzi, L., Cresci, G., Telles, E., & Melnick, J. 2008, *A&A*, **486**, 393
- Vanzi, L., Hunt, L. K., & Thuan, T. X. 2002, *A&A*, **390**, 481
- Vanzi, L., Hunt, L. K., Thuan, T. X., & Izotov, Y. I. 2000, *A&A*, **363**, 493
- Vanzi, L., & Sauvage, M. 2004, *A&A*, **415**, 509
- Walter, F., Brinks, E., de Blok, W. J. G., Bigiel, F., Kennicutt, R. C., Thornley, M. D., & Leroy, A. 2008, *AJ*, **136**, 2563
- Whitmore, B. C., et al. 2005, *AJ*, **130**, 2104
- Wolfire, M. G., Hollenbach, D., & McKee, C. F. 2010, *ApJ*, **716**, 1191
- Wolfire, M. G., McKee, C. F., Hollenbach, D., & Tielens, A. G. G. M. 2003, *ApJ*, **587**, 278
- Wong, T., & Blitz, L. 2002, *ApJ*, **569**, 157
- Young, J. S., Xie, S., Kenney, J. D. P., & Rice, W. L. 1989, *ApJS*, **70**, 699